

Chapter 2

Experiment Details

2.1 Vacuum System

The apparatus (Figure 2.1.1) consisted of three differentially pumped chambers. The layout of these chambers and the vacuum pumps is shown, in detail, in Figure 2.1.2. The entire apparatus sat on a horizontal rail and was opened by decoupling the forelines and sliding each chamber along the rail.

The first chamber (expansion chamber) housed the pulsed nozzle valve, pyrolysis tube and the skimmer (Figure 2.1.3). This chamber was evacuated by a 4400 ls^{-1} , 10" diffusion pump (Varian VHS10) that was cooled by recirculating water from a header tank through the cooling coil. A pneumatically-operated gate valve was positioned between the VHS10 and the expansion chamber so that the pump could be isolated from the chamber. The VHS10 was backed by a rotary pump (Balzers DUO 060A), which was also used to rough the expansion chamber when pumping down from atmosphere (Figure 2.1.4).

The pressure in the expansion chamber was monitored by a full-range, Bayard-Alpert type ionisation gauge (Balzers PBR260) while a Pirani gauge (Balzers TPR265) monitored the pressure in the VHS10 foreline. The rotary pump was trapped by a -30°C refrigerated cold finger placed in the foreline to minimise any back streaming of oil into this chamber.

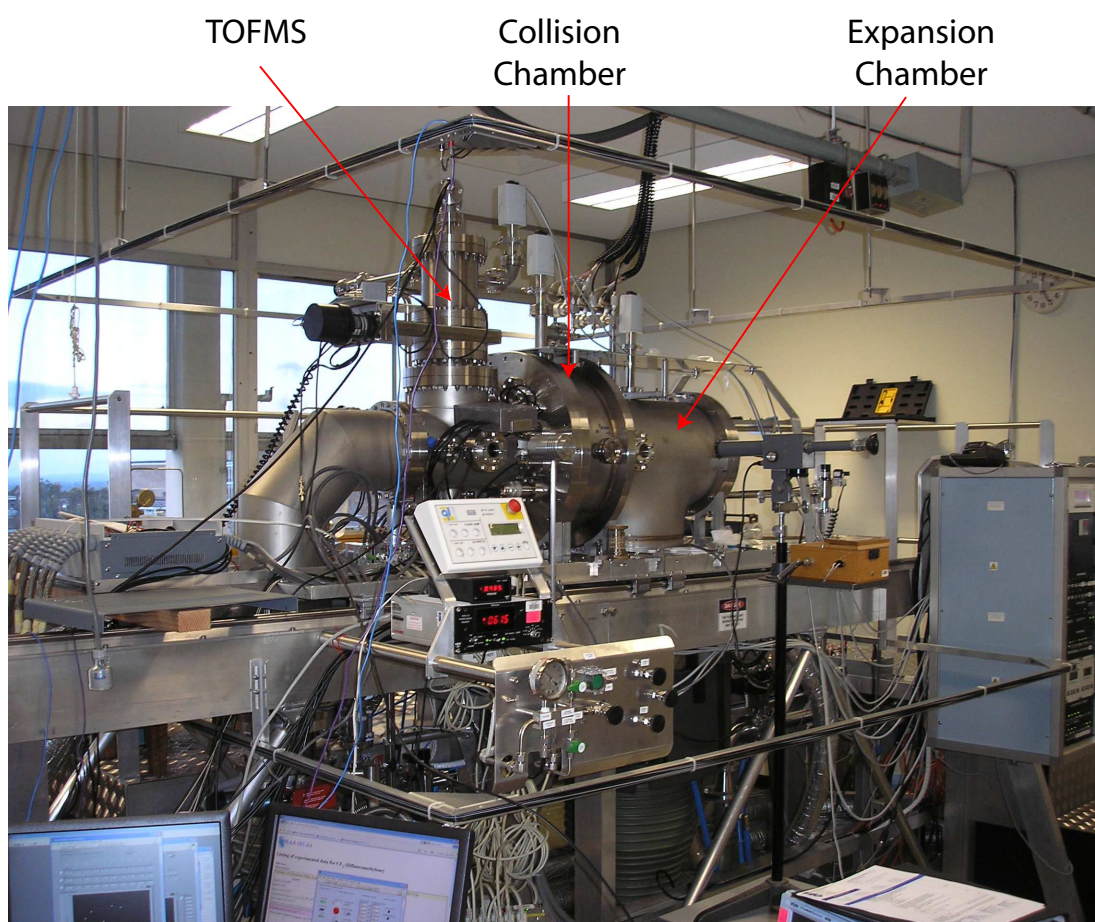


Figure 2.1.1: A photograph of the present apparatus with some of its important sections being labelled on the figure. The collision chamber also incorporates a differentially pumped monochromator chamber.

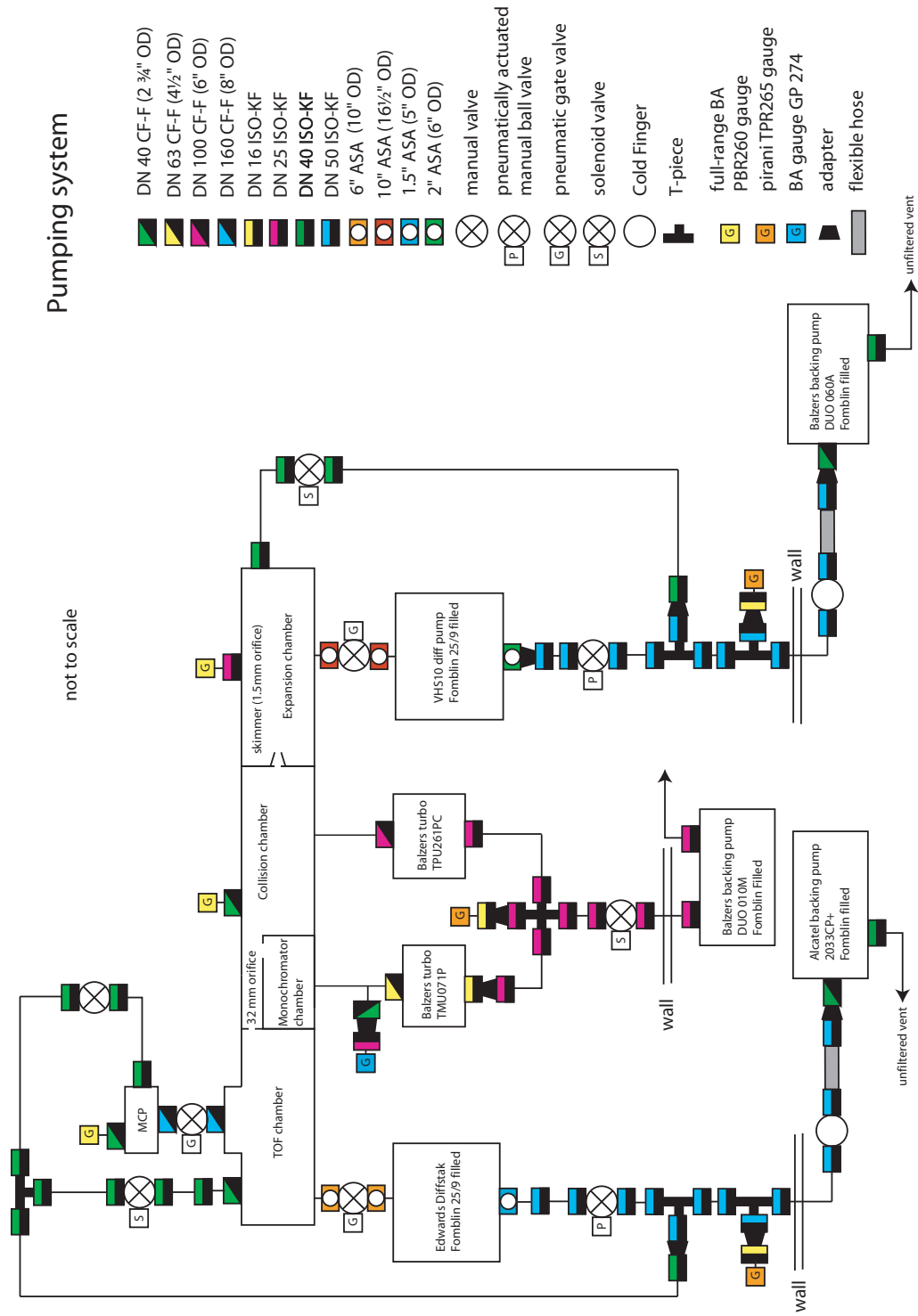


Figure 2.1.2: A schematic diagram of the pumping system employed in the present experiment.

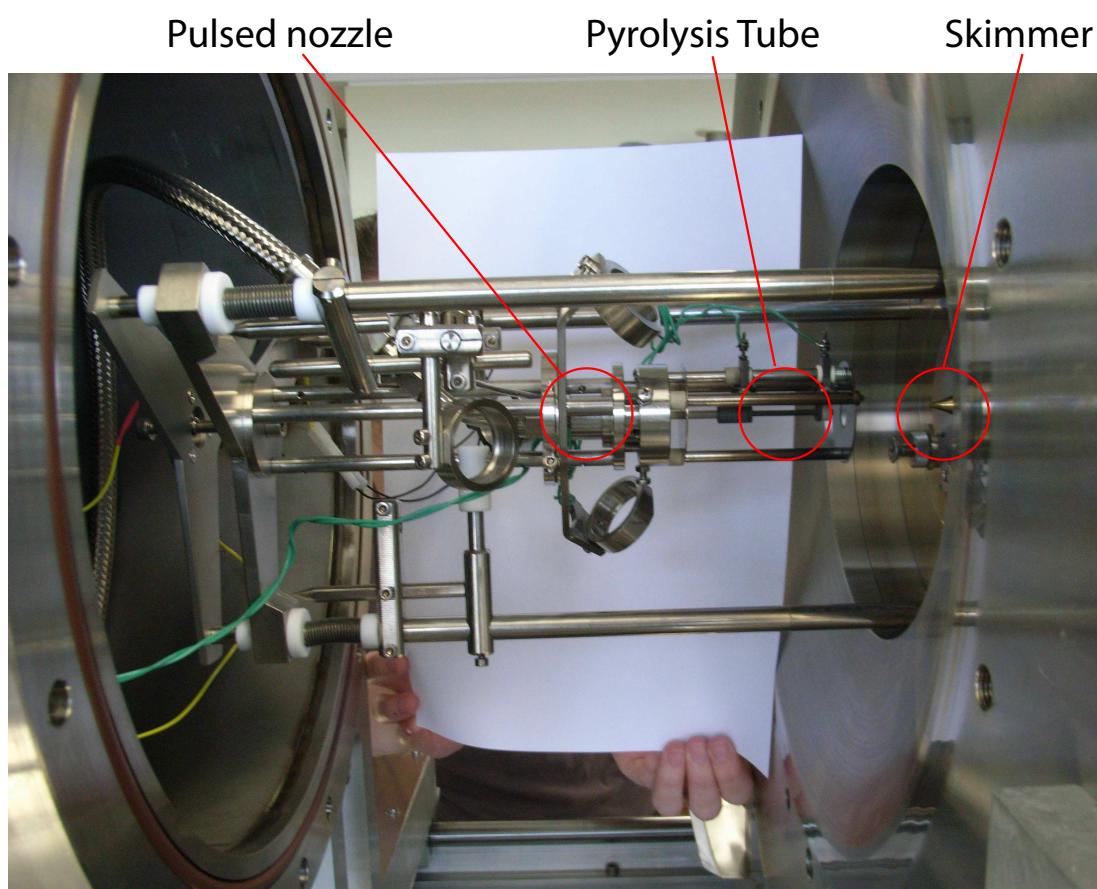


Figure 2.1.3: An internal photograph of the expansion chamber, showing the pulsed nozzle, pyrolysis tube and skimmer.

The second chamber (collision chamber), separated from the expansion chamber by the skimmer, housed the electron monochromator and electron detection array (Figures 2.1.5 and 2.1.6). The monochromator itself was positioned inside a differentially pumped housing within the collision chamber, and one end of the monochromator cylinder lens stack (Section 2.3.1) protruded through this housing in order to allow the electron beam to cross the molecular beam. The differential pumping allowed the monochromator to operate under a lower pressure than the main collision chamber when gas was introduced into the system, thus preserving the filament. This housing was also used to ensure the performance of the monochromator was stable when reactive gases were used in the system.

The collision chamber was evacuated by a 190 ls^{-1} turbomolecular (turbo) pump (Balzers TPU 261PC), while the monochromator housing was evacuated by a second turbo (Balzers TMU 071P) of pump speed 33 ls^{-1} . Both of the turbos were air-cooled by electric fans, as well as by flowing mains water through the stainless steel cooling block. These turbos were backed by a single, untrapped, rotary pump (Balzers Duo 010M). The pressure in the collision chamber was monitored by a full range Bayard-Alpert gauge (Balzers PBR260), while the monochromator chamber pressure was also monitored with a Bayard-Alpert type ionisation gauge (Granville-Phillips series 274). The pressure in the turbo's foreline manifold was monitored with a Pirani gauge (Balzers TPR265).

The third and final chamber (TOF chamber) of the apparatus, separated from the collision chamber by a 30 mm orifice, housed the extractor and repeller plates and microchannel plate detectors used for the time-of-flight mass spectrometer. The TOF chamber was evacuated by a 700 ls^{-1} diffusion pump (BOC Edwards Diffstak 160/700), which was cooled by flowing water from the header tank through the pump's cooling coils. A pneumatic gate valve was positioned between the Diffstak and TOF chamber to isolate the pump from the vacuum chamber. The Diffstak was backed (Figure 2.1.4) by a trapped rotary pump

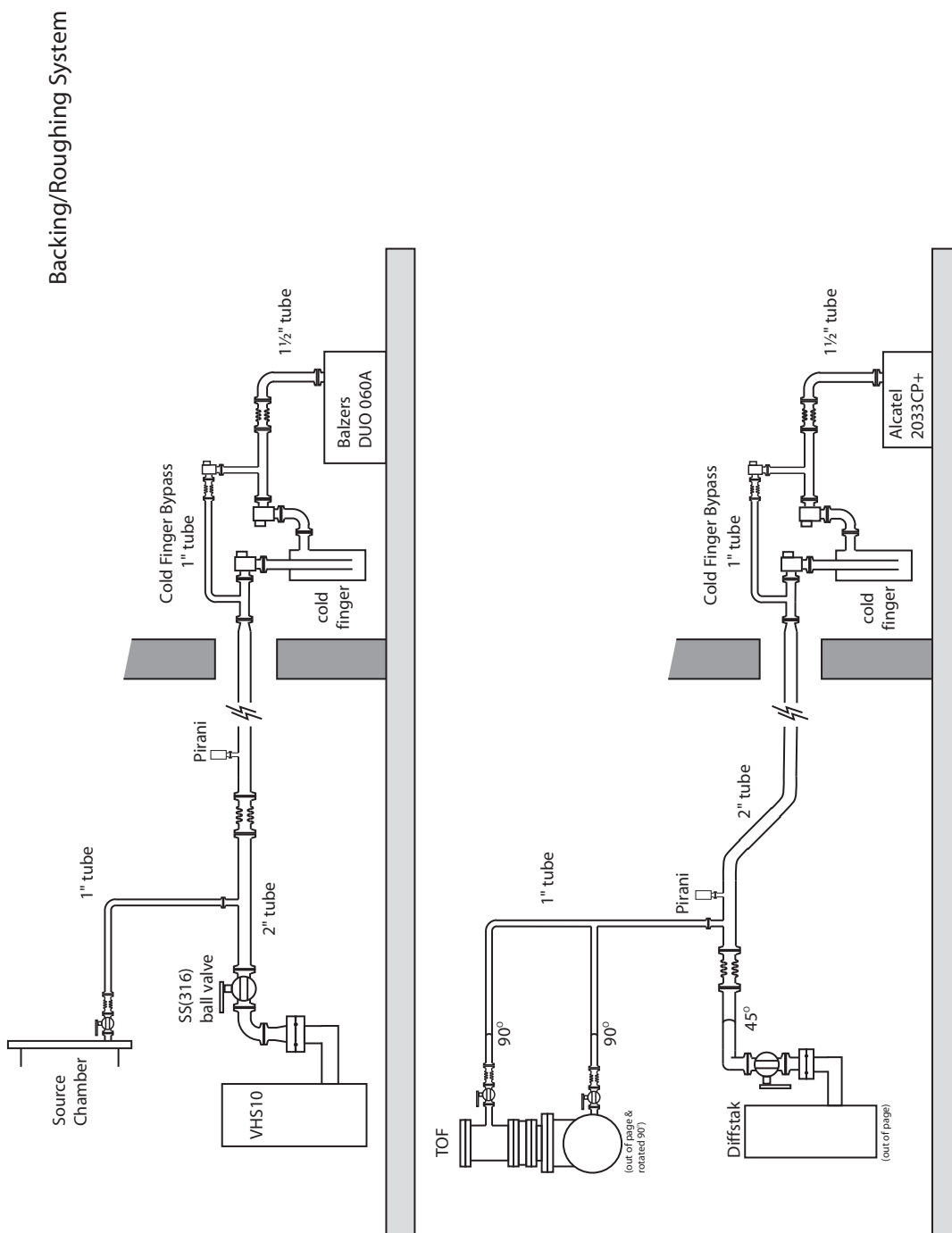


Figure 2.1.4: A schematic diagram depicting two of the backing pumps and showing their role in the present experiment.

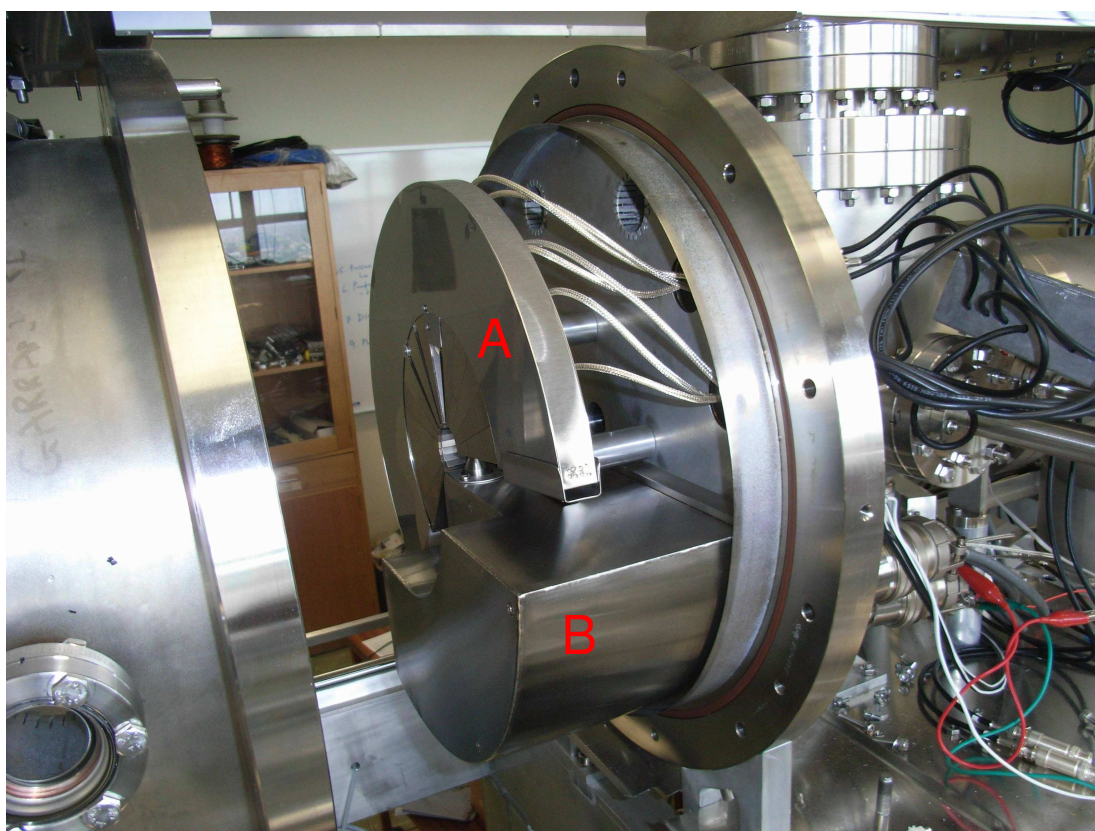


Figure 2.1.5: An internal photograph of the scattering chamber, showing the electron detection array (A) and differential pumping housing for the monochromator (B).

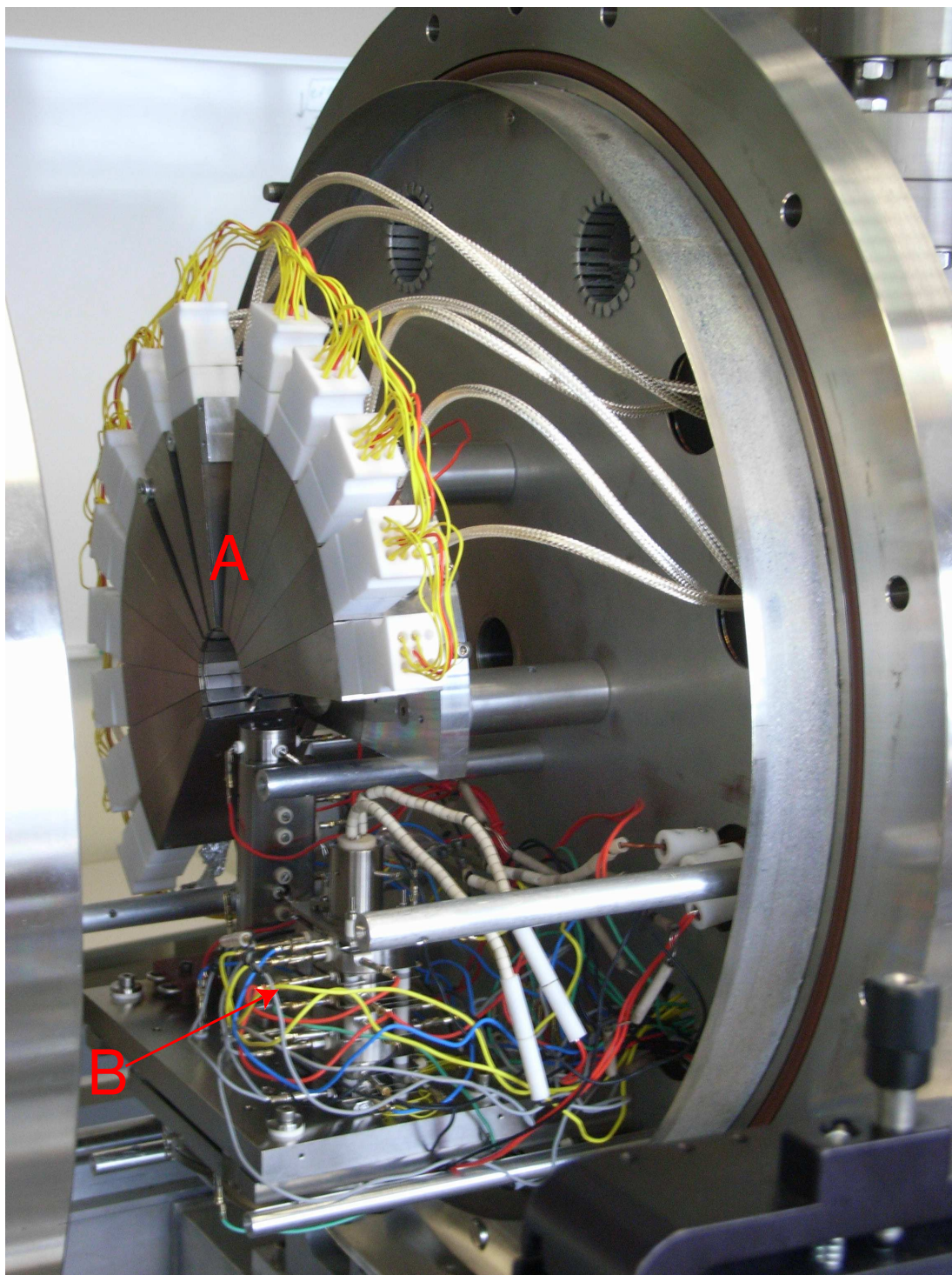


Figure 2.1.6: An internal photograph of the scattering chamber, again showing the electron detection array (A) and electron monochromator (B). The monochromator differential pumping housing and electron detector shielding has been removed for the photograph.

(Alcatel 2033CP+). The pressures in the TOF chamber and Diffstak foreline were monitored by a full range gauge (Balzers PBR260) and Pirani gauge (Balzers TPR265) respectively.

Both the VHS10 and the Diffstak were fitted with cold traps to prevent pump oil backstreaming into the vacuum chamber. These traps were cooled by a commercially purchased recirculating methanol chiller (Thermoline), which was custom made for the present apparatus. The chiller cooled an 80l bath of methanol to approximately -80°C using a two stage, cascade compressive refrigerator unit, with ethane used as the refrigerant gas. Once cooled the methanol was continuously recirculated through the two cold traps, which were connected in series, using a submersed electrical pump (Lowara SVI). The methanol was transported to the cold traps by stainless steel tubing lagged with two layers of high density, foil encased foam, which minimised the ambient heat load on the cooling lines. Whilst circulating the methanol bath indefinitely maintained a temperature of -70°C in the cold traps. This temperature, whilst higher than that of liquid nitrogen (which is often used to charge cold traps), was adequate to prevent diffusion pump oil backstreaming into the apparatus and also to maintain the pumping speeds.

Also, by avoiding the use of liquid nitrogen, a significant saving in the operational costs of the apparatus was achieved. The VHS10 cold trap alone would have consumed approximately 7 litres per hour of liquid nitrogen, which was sold by the university at AU\$1.50 per litre. With continuous operation of the system, this equalled an expenditure around AU\$61,320 per year for liquid nitrogen, thus easily justifying the initial AU\$20,000 outlay on the methanol chiller.

To minimise the noise and heat in the laboratory, the rotary pumps and the methanol chiller were kept in a separate room from the rest of the experiment. All of the vacuum pumps in the system were charged with perfluorinated oils (Fomblin or F5) to allow corrosive gases to be used in the system.

2.1.1 Programmable Logic Controller

Each of the vacuum pumps for the apparatus was controlled by a programmable logic controller (PLC). In addition, the gate valves, solenoid valves and pneumatically-actuated ball valves to the chamber, pumps and forelines were also all controlled from the PLC. A photograph of the PLC front panel is given in Figure 2.1.7, which shows the controller for the pressure heads (Pfeiffer Maxigauge) located in the top panel, the turbo controllers, system status readouts and the temperature readout. The Maxigauge simultaneously displayed the readouts from the three Pirani gauges and the three Bayard-Alpert gauges. The other pressure gauge controller (Granville-Phillips 307), monitoring the monochromator chamber pressure, was mounted separately in a different rack.

As well as providing a centralised method for controlling the experiment, the PLC automatically shut the experiment down in the event of a fault condition. Such a fault condition was generated if the PLC detected: a large pressure rise in the chamber; an interruption (or overload) to the power or water supplies; a large temperature rise in the chilled methanol bath; or, if the safe operating temperature of a diffusion pump was exceeded. When a fault condition was detected, the PLC closed the gate valves to protect the diffusion pumps and channel plate detectors and deactivated the vacuum pumps. Furthermore, the high voltage supplies to the TOF's extractor and repeller, the channel plate detectors and the array of channel electron multipliers were deactivated, as were the voltage supplies to the electron monochromator and the monochromator filament current. Finally, the solenoid valves of the gas handling system (Section 2.2.2) were closed so that gas was no longer admitted into the system.

2.2 Pulsed Gas Source

2.2.1 Pulsed nozzle

Gas was introduced to the vacuum system through a stainless steel pulsed nozzle (Figure 2.2.1), fitted with a SiC tube for the pyrolysis. The pulsed nozzle valve



Figure 2.1.7: A photograph of the programmable logic controller and the Pfeiffer Maxigauge pressure monitoring controller, turbo controllers and temperature readout.

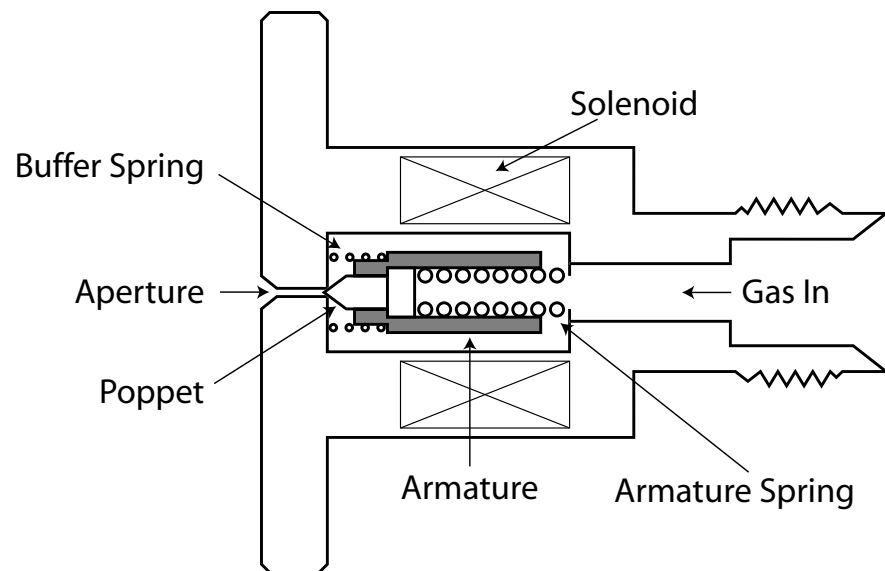


Figure 2.2.1: A schematic diagram of the pulsed nozzle valve.

was a normally closed, magnetic solenoid valve (Parker Hannifin, General Valve Series 9). The nozzle aperture size was usually 0.5 mm, although alternative nozzles between 0.1 mm and 1 mm diameter were also used. The nozzle was sealed with a Teflon poppet, seated inside a magnetic armature, which in turn was seated inside a solenoid. The armature was magnetically retracted by passing a pulsed current through the solenoid and subsequently closed by the armature spring. The resistance of the coil was $3\ \Omega$; this resistance was chosen to allow gas pulses $<100\ \mu\text{s}$ in duration [45] to be generated. The duration of the gas pulses was, however, typically $\sim 2\ \text{ms}$ in the experiments reported in this thesis. Nonetheless, this coil resistance was chosen in case shorter gas pulses were required in future. Experiments to measure the pulse width are described in Appendix C.1.

The current for the pulser solenoid was supplied using a pulsed nozzle driver that was manufactured in-house (Flinders University, School of Chemistry, Physics and Earth Sciences Electronics Workshop). The pulsed nozzle driver was triggered at a repetition rate of 10 Hz, and the output pulses were between 100-400 μs in duration with amplitudes between 10-60 V DC (3-20 A). The rise and fall times of these driving pulses was $\sim 50\ \text{ns}$ to ensure the opening and closing times of the pulser were as short as possible. The pulsed nozzle driver allowed the amplitude and duration of these current pulses to be manually varied.

A skimmer (Beam Dynamics Model 1) was positioned 50 mm downstream of the nozzle (Figure 2.2.2), to produce a collimated gas pulse for the electron scattering studies. The skimmer, located 50 mm from the nozzle, was 1.92 cm long, 2.22 cm in diameter at the base and had a 1.5 mm orifice at the apex. A gold plated double walled Cu skimmer was chosen so that the skimmer was strong, non-magnetic and resistant to corrosive gases. The skimmer was specifically designed for use with supersonic gas jets featuring thin walls (10 μm each at the apex and 50-80 μm each at the wall and base) and a small angle at the orifice (25°) to minimise any backscattering of the jet particles.

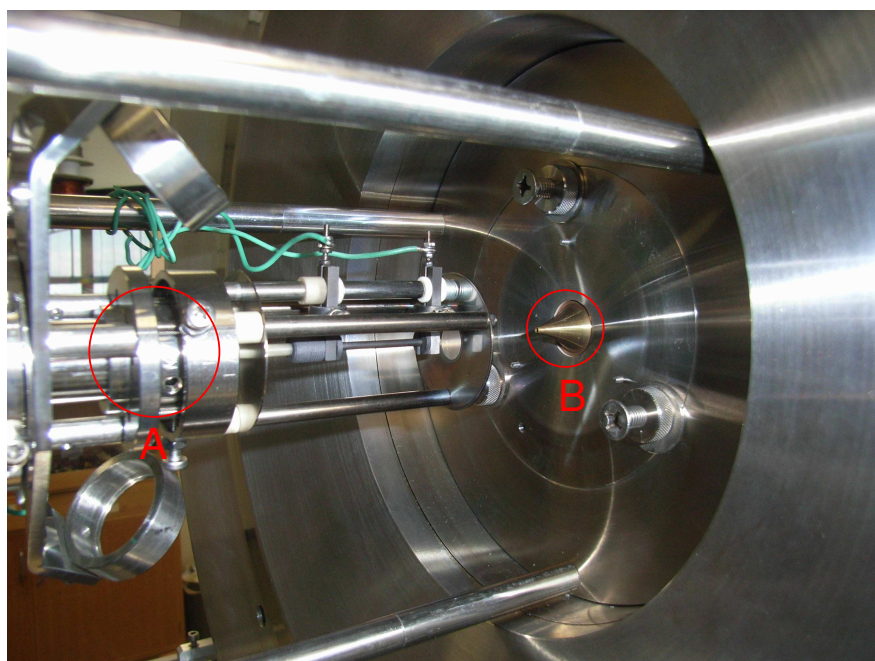


Figure 2.2.2: An internal photograph of the pulsed nozzle (A) and skimmer (B).

2.2.2 Pyrolysis Nozzle

A pyrolytic nozzle, based on a previously reported design [35], was mounted to the front of the pulsed nozzle (Figure 2.2.3) to generate the CF_2 radicals. The pyrolysis tube, manufactured from SiC (Hexoloy), had an inner diameter (ID) of 1 mm, outer diameter (OD) of 2 mm and was 37 mm long. The pyrolysis nozzle was supported by two pairs of split graphite bushes held in titanium clamps. The titanium clamps were connected to an Al_2O_3 insulator, and separated by a stainless steel studding. The clamp at the exit of the tube was free to move along the studding in order to accommodate the expansion of the pyrolysis tube when heat was applied. A spring was positioned between the free clamp and one end of the nozzle assembly to stabilise the nozzle.

Two stainless steel heat shields were positioned 4 mm either side of the SiC tube to shield the pulsed nozzle and other components from being radiantly heated by the tube. These heat shields were supported by three stainless steel posts, 68 mm in length, which were in turn supported from a stainless steel faceplate mounted to the front face of the nozzle. The heat shields were separated from the nozzle by a Al_2O_3 tube (length 32 mm, ID 2 mm).

The pyrolysis tube was initially annealed to lower the resistivity of the SiC. This was achieved by applying an AC voltage (approximately 20 V) across the SiC, which was simultaneously heated by a nichrome wire filament at a temperature of 2000°C. The resistance of the SiC tube is approximately 400 Ω at room temperature. However, this resistance reduced to approximately 10 Ω when the SiC reached 1800°C. Once the tube reached this temperature, the SiC annealed and was thereafter able to self-ignite when a sufficient AC voltage was applied.

Once annealed, the pyrolysis tube was electrically heated by applying an AC voltage using a 240 V, 5 A Variac (Berco 71A), which was connected to an isolation transformer. The electrical connections were made using the graphite bushes, with the Variac being connected across the two ends of the SiC tube. The con-

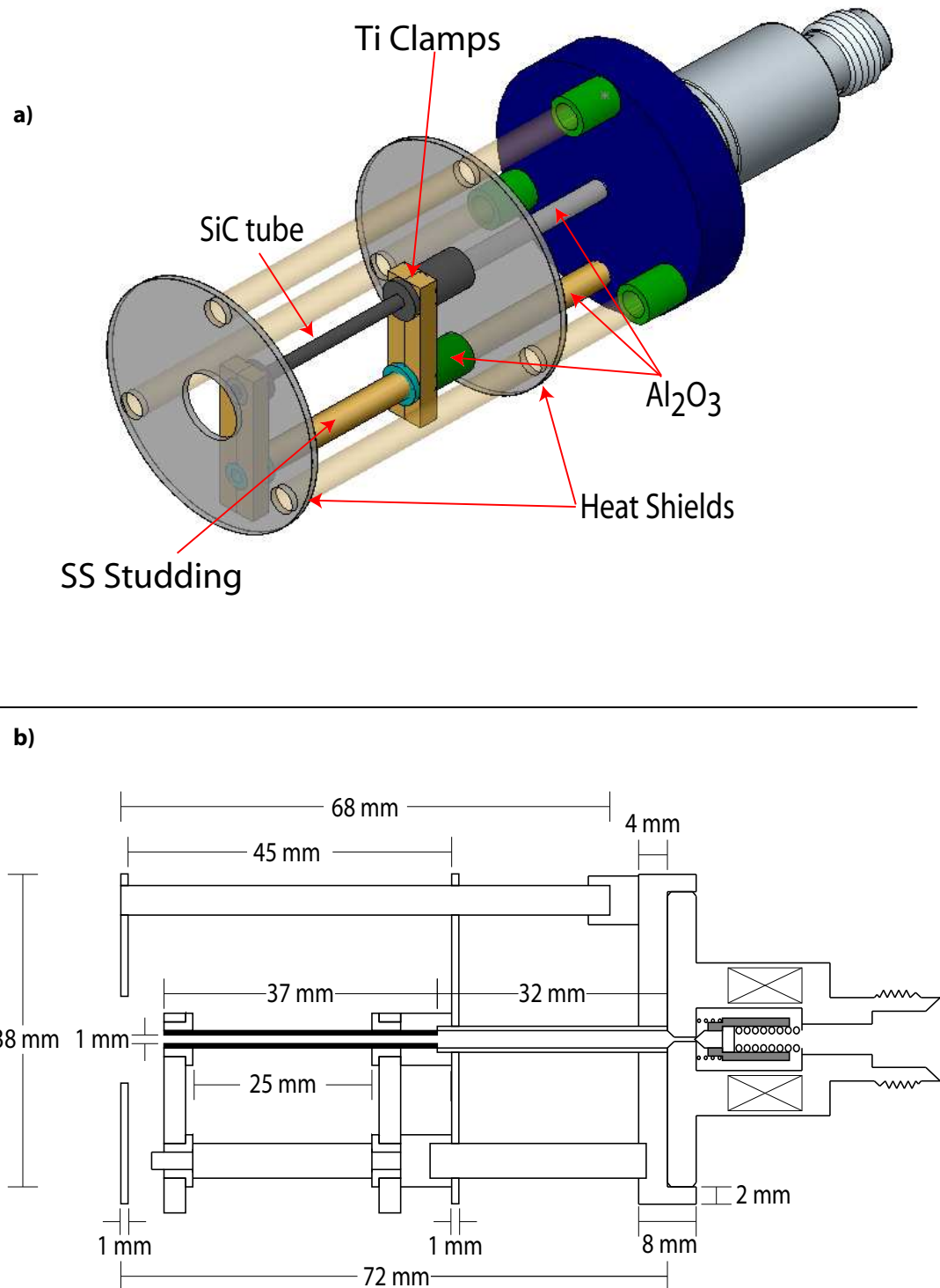


Figure 2.2.3: Pictorial representation (a) and schematic diagram (b) of the pulser with the pyrolysis nozzle fitted.

duction path through the nozzle was provided by the titanium clamps. The temperature of the tube was monitored with a calibrated optical pyrometer, which viewed the pyrolysis tube through the expansion chamber view port. The pyrometer covered a temperature range of 700°C to 2500°C.

Gas Handling System

Gas cylinders were connected to the pulser via a gas handling system (GHS) (Figures 2.2.4 and 2.2.5). The current design allowed two gas cylinders to be connected simultaneously to the GHS, with the gases routed as required. The GHS was manufactured from 1/4" stainless steel tubing, which connected a series of manual valves, 24 V DC solenoid valves (SMC XSA1-125), needle valves and variable leak valves (Granville Phillips type 203). The connections used to facilitate this in the GHS were predominantly 1/4" Swagelok. The GHS was mounted onto a stainless steel backing plate, which in turn was secured to the laboratory wall.

Gas flow was routed through the GHS by the solenoid valves, which were controlled by a dedicated PLC, and metered by the needle valves and variable leak valves. A 1000 Torr High-precision Baratron (MKS 122A) was used to monitor the stagnation pressure of gas behind the pulsed nozzle. The GHS was evacuated as necessary by the Balzers 060A rotary pump.

Two reservoir tanks were included in the GHS to allow the option of decanting gas from the cylinders into the reservoirs, rather than being routed straight to the back of the pulsed nozzle. This option allowed gas samples to be prepared at lower pressure than a regulated gas cylinder, or for samples of gas mixtures to be prepared. The pressure in each of these reservoirs was monitored by 1000 Torr Baratrons (MKS 120).

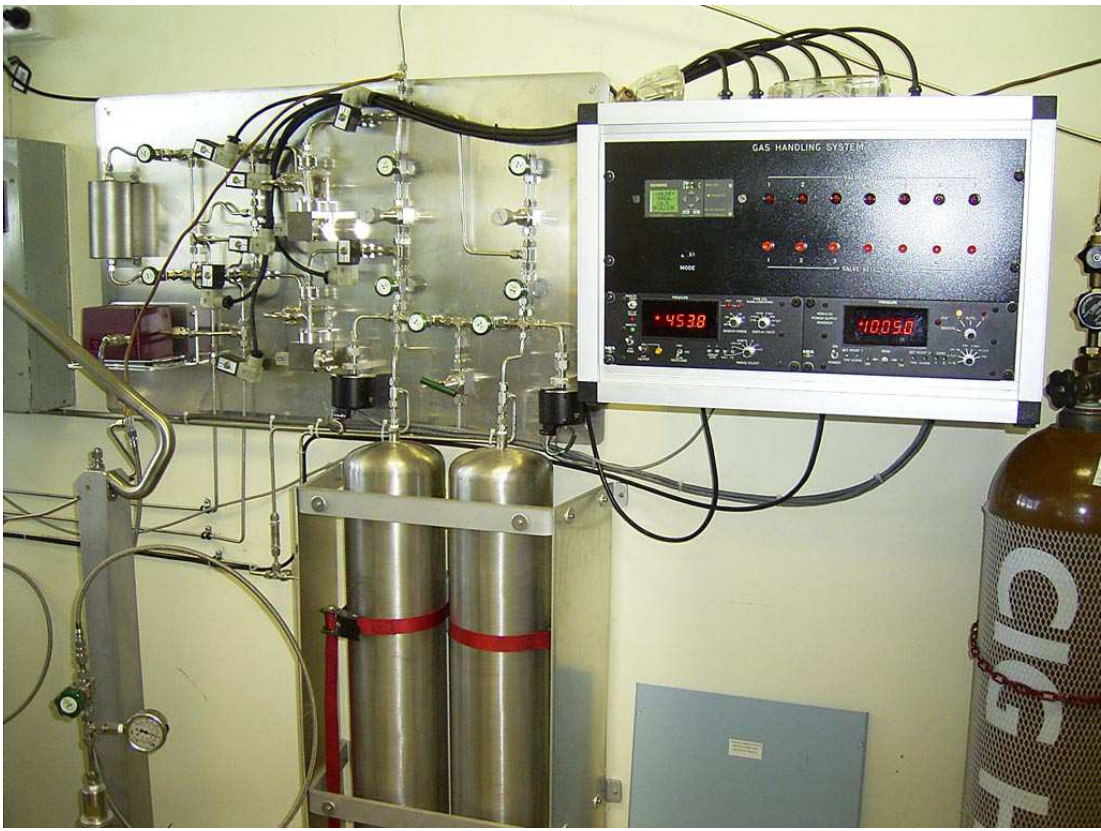


Figure 2.2.4: A Photograph of the present gas handling system.

Gas Handling System

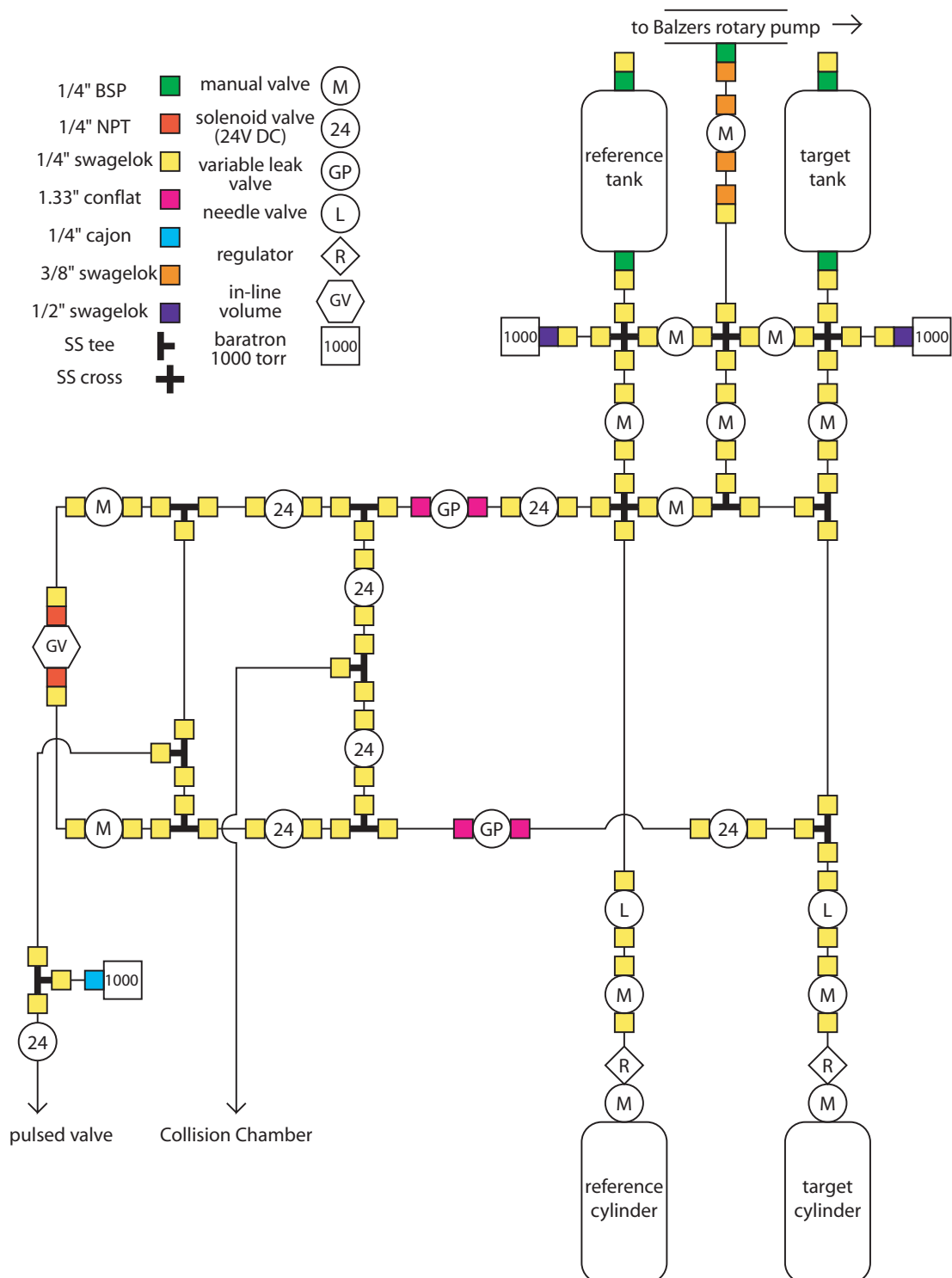


Figure 2.2.5: A schematic diagram of the gas handling system. The acronym SS stands for stainless steel.

2.3 Electron Monochromator and Detectors

The skimmed gas pulse from the expansion chamber was crossed at 90° with a focussed electron beam of known energy (0.5-50 eV) and low energy spread (<150 meV). The electron beam was produced by a hemispherical electron monochromator, incorporating both aperture- and cylindrical-type lenses to transport and focus the electrons. Angular distributions of elastically scattered electrons were measured by an array of 13 fixed-position electron detectors, covering an angular range of -75° to 135° about the interaction region. Each individual detector unit contained a retarding field analyser (RFA), so that only electrons which scattered elastically reached the electron detector. The electron beam current was also monitored using two concentric Faraday cups, referred to as the inner and outer cups. The configuration of the monochromator and detectors is shown in Figure 2.3.1.

2.3.1 Electron Monochromator

The electron monochromator (Figure 2.3.2) consisted of two separate electrostatic lens modules, denoted as the aperture lens stack and cylinder lens stack, and a hemispherical energy selector, all mounted off a titanium baseplate. All the materials used in the construction of the monochromator were non-magnetic and bakeable. The monochromator baseplate, off which the lens stacks were mounted, was connected to two support brackets which were mounted to the scattering chamber flange. Note that the baseplate was electrically insulated from these brackets by Al_2O_3 spacers.

Aperture Lens Stack

The aperture lens stack (Figure 2.3.3) was used to transport and focus electrons between the electron source and the energy selector. Electrons were produced by thermionic emission from a thoriated tungsten hairpin filament in a triode configuration. The apex of the filament sat flush with the back of a pierce extraction element and electrons were extracted onto a 1 mm aperture (anode). Electrons were emitted from the filament and focussed onto the entrance plane

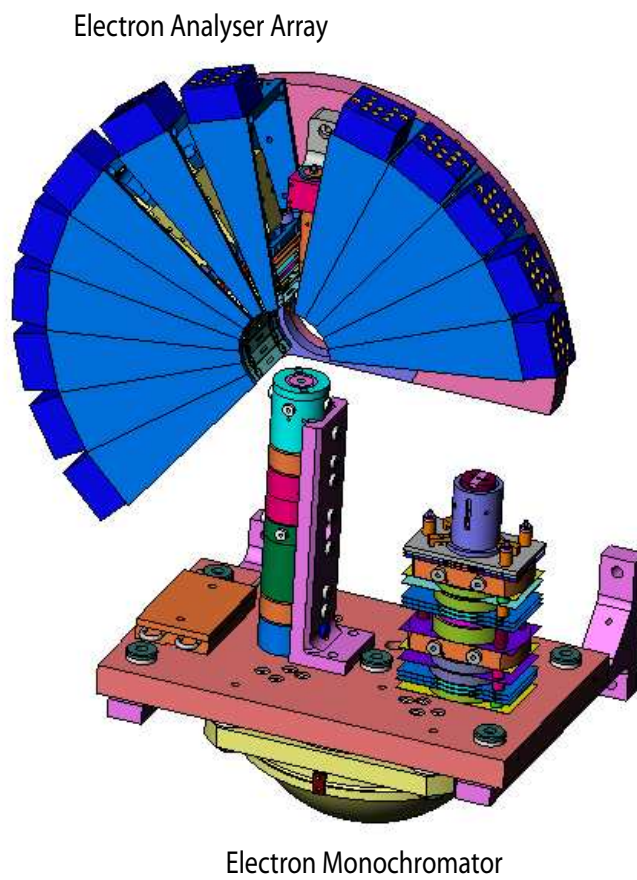


Figure 2.3.1: Pictorial representation of the experimental geometry for the electron scattering section of the apparatus. Shown are the electron monochromator and the multi-detector array.

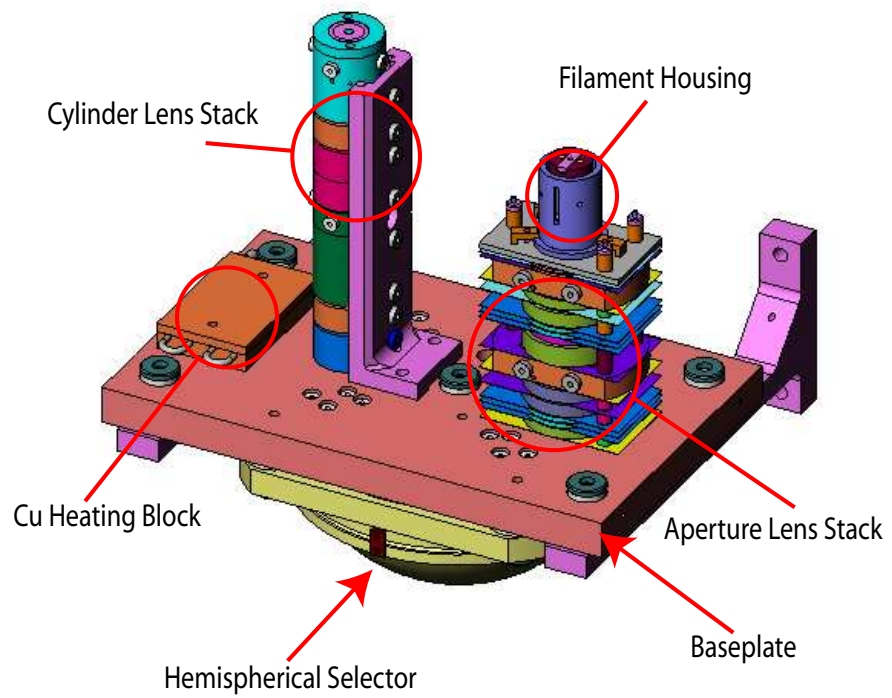


Figure 2.3.2: Pictorial representation of the electron monochromator.

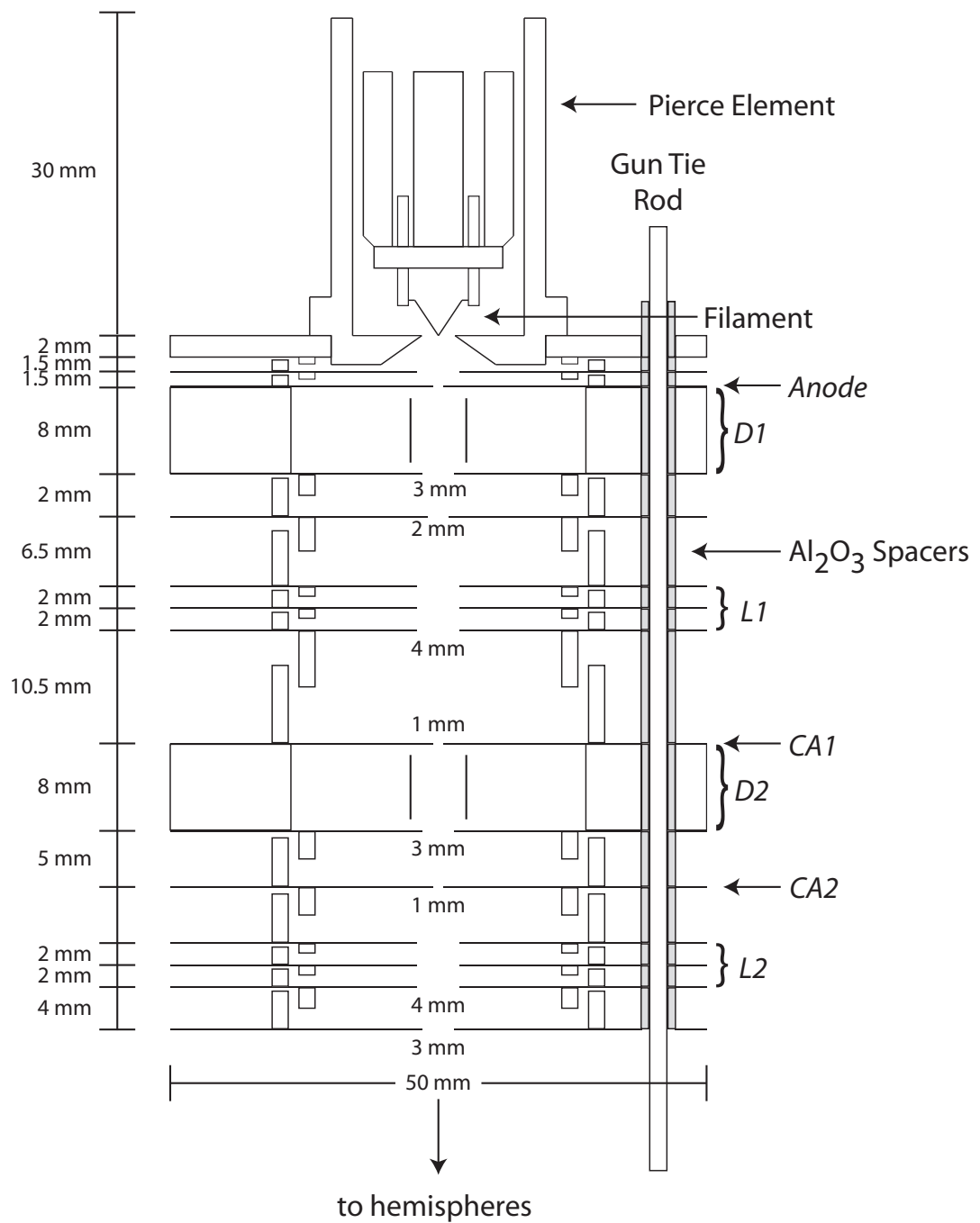


Figure 2.3.3: A schematic diagram of the aperture lens stack. The deflectors (D1/D2), lenses (L1/L2) and collimating apertures (CA1/CA2) are all shown. Also shown are the spacings between the various electron optic elements and the aperture sizes associated with these elements.

of the energy selector by two sets of three-element retarding lenses ($L1/L2$) of aperture-type geometry ($A/D \approx 0.5$, where A is the spacing between the lens elements, 1.9 mm, and D is the diameter of the lens aperture, 4 mm), with a field free region between them. The design of the aperture lens stack incorporated two collimating apertures ($CA1/CA2$), to ensure the beam had a small pencil half angle at the selector entrance. The electron beam was steered through this stack by two sets of deflectors ($D1/D2$).

The apertures and lens elements used in this lens stack were constructed from 0.15 mm thick titanium sheets and separated from each other by Al_2O_3 spacers (Small Parts). The aperture lens stack was held together by three threaded support posts, which ran down the centre of the Al_2O_3 spacers. These support posts were screwed directly into the baseplate. The respective sizes of the lens apertures and the separations between the respective lens elements are given in Figure 2.3.3. Note that all the individual lens elements and collimating apertures had titanium cylinders spot welded to them, in order to shield the Al_2O_3 spacers from the electron beam. Had the spacers been exposed to the electron beam they may have accumulated charge, which would adversely affect the performance of the electron optics.

Hemispherical Selector

Electrons leaving the aperture lens stack had an energy resolution of approximately 500 meV due to the thermal energy spread from the heated filament, and so a hemispherical selector (Figure 2.3.4) was used to improve the energy resolution of the primary beam. The selector consisted of two concentric hemispheres both commercially spun from titanium. The radius of the inner hemisphere (r_1) was 30 mm, while the outer hemisphere radius (r_2) was 50 mm. The energy selector therefore had a mean radius (r_0) of 40 mm.

The selector also incorporated four field correction electrodes at the open edges of the hemispheres, so that the electric field more closely approximated the $1/r^2$ type that would be present if complete spheres were used. These electrodes

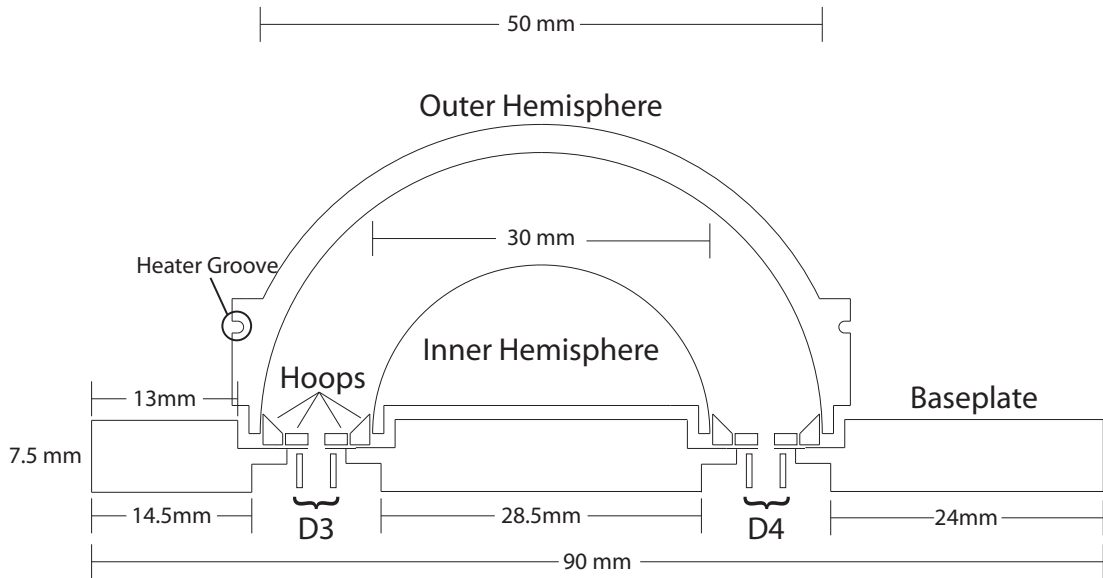


Figure 2.3.4: A schematic diagram of the Hemispherical Selector.

took the form of hoops which sat concentrically with the hemispheres. These hoops were manufactured from type-310 stainless steel and seated on PTFE spacers which were attached to the baseplate. The hoops and hemispheres were electrically insulated from the monochromator baseplate by Al_2O_3 spacers (Small Parts).

Two deflectors ($D3/D4$) were also incorporated into the selector design, located immediately before the entrance and exit planes of the hemispheres. These deflectors were used to increase the electron throughput of the selector by correcting for any non-paraxial ray focussing of the electron beam.

Cylindrical Lens Stack

The cylindrical lens stack (Figure 2.3.5) transported electrons from the exit plane of the hemispherical selector to the interaction region. This stack incorporated two sets of three element lenses with cylindrical symmetry ($L3/L4$, $A/D=1$ where A is the lens width, 4 mm, and D is the lens diameter, 4 mm), with a field-free region between them that incorporated two collimating apertures ($CA3/CA4$), again constructed from 0.15 mm thick titanium foil. Two sets of deflectors ($D5/D6$) were included in this lens stack to help steer the electron beam. The

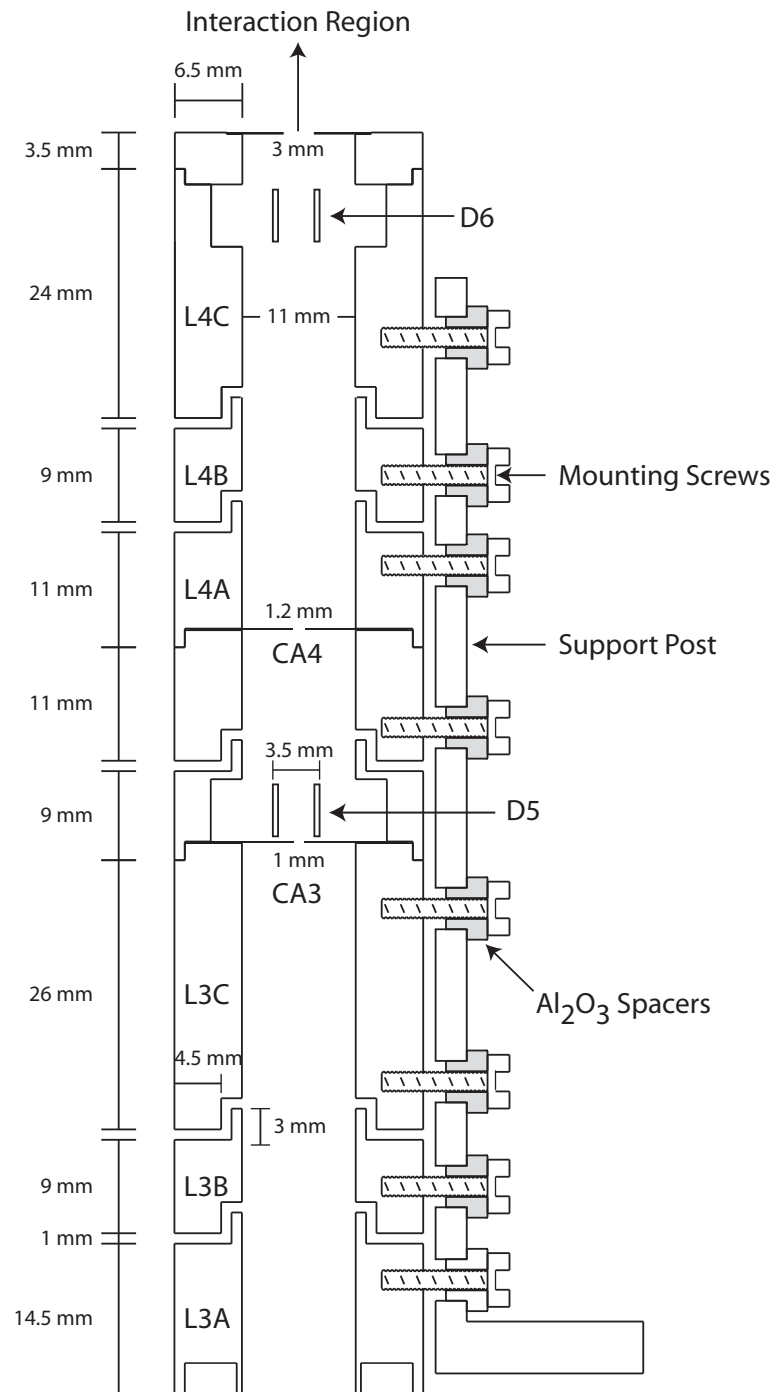


Figure 2.3.5: A schematic diagram of the cylinder lens stack. The deflectors ($D5/D6$), lenses ($L3/L4$) and collimating apertures ($CA3/CA4$) are all shown. Also shown are the spacings between the various electron optic elements and the aperture sizes associated with these elements.

cylindrical lenses were mounted from a titanium support post, with the mounting screws insulated from this post by Al_2O_3 spacers (Small Parts). This support post was mounted directly off the baseplate, and the cylindrical lenses were isolated from this post by 1.6 mm diameter glass rods that ran the length of the support post.

Faraday Cups

The electron beam from the monochromator was monitored by two cylindrical Faraday cups, denoted inner and outer, respectively (Figure 2.3.6). The inner (1.25 mm radius, 6 mm length) and outer cups (4 mm radius, 55 mm long) were located 40 mm from the end of the cylinder lens stack and they were both knife-edged to try and prevent backscattering of electrons into the interaction region. The outer cup was held in a custom mount (Figure 2.3.6) which was mounted directly to the analyser baseplate. The outer cup was insulated from this mount by PTFE. The inner cup was insulated from the outer cup using custom made PTFE spacers, which also supported the inner cup within the outer. The Faraday cups were made from type 310 stainless steel to ensure they were non-magnetic. The currents on the inner (I_{inner}) and outer (I_{outer}) Faraday cups were measured by independent picoammeters (Keithley 485 and 480 respectively).

Monochromator Control Electronics

The potentials to the cathode, lenses, deflectors, hemispheres, hoops and apertures were generated from custom made (Electronics Workshop, Research School of Physical Sciences and Engineering, ANU), computer-interfaced voltage/current supplies; aspects of these supplies are summarised in Table 2.1. The voltage supplies were all stable to $<10\text{ mV}$ and were controlled by a 3.6 GHz Pentium-4 PC, running Windows XP, with communication to the supplies via an optically isolated, single wire, serial communications bus using an SAE J1850 protocol. The software to drive these voltage supplies was written in a commercial code (LabView 8.0), and all of the necessary LabView software was developed during the course of this thesis work.

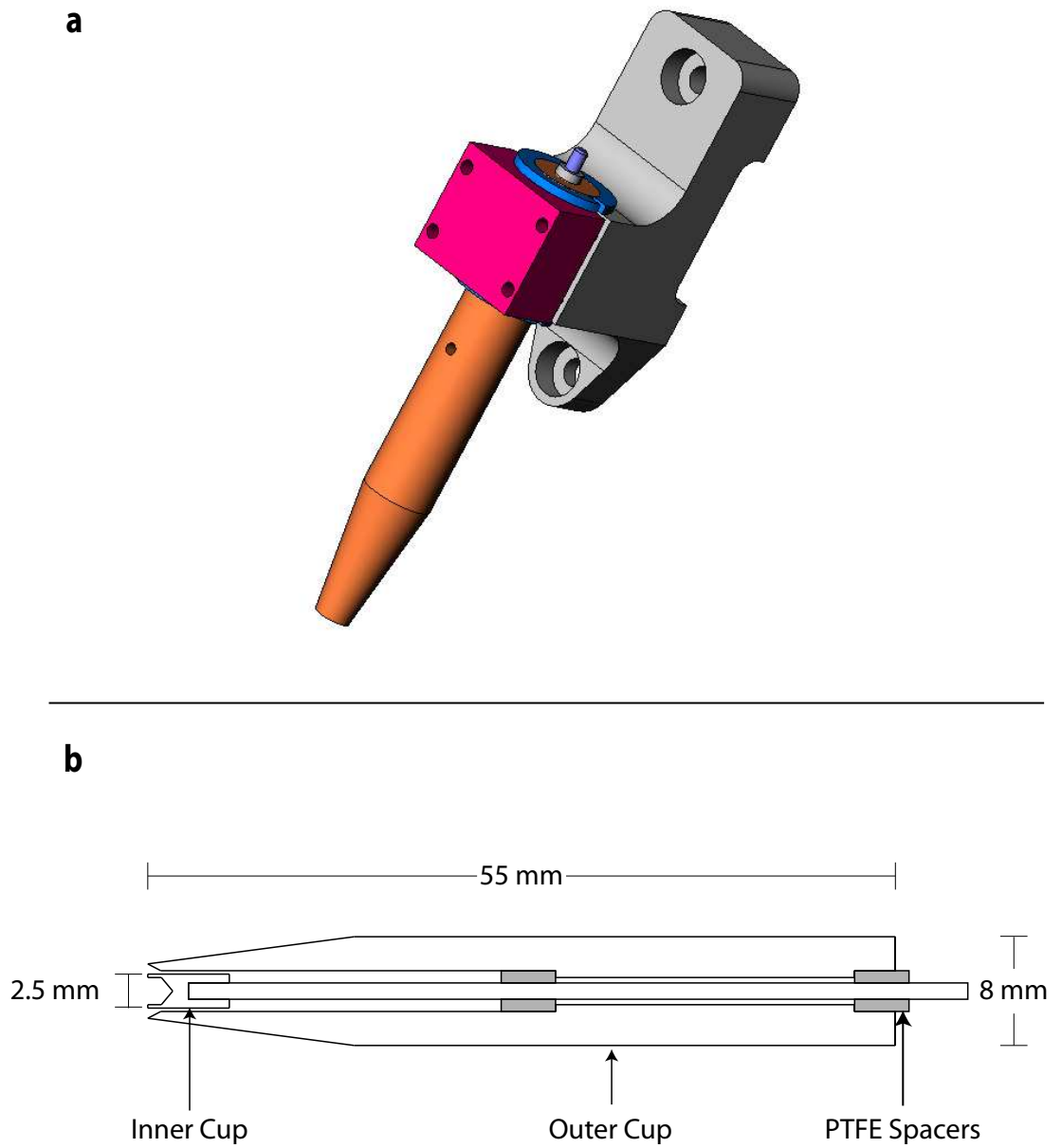


Figure 2.3.6: Pictorial representation a) and schematic diagram b) of the Faraday Cups.

Table 2.1: Details for each of the present monochromator voltage supplies. Y (yes) or N (no) denotes whether a voltage supply was bipolar or had a current pickup.

Supply Name	Max. Voltage	Bipolar	Current Feedback
Beam Energy	-50	N	N
Contact Potential	1	Y	N
Pierce Element	3	Y	N
Grid	50	N	N
Anode	150	N	Y
Deflector 1X	25	Y	N
Deflector 1Y	25	Y	N
Lens 1B	300	N	N
Lens 1C	50	N	Y
Deflector 2X	25	Y	N
Deflector 2Y	25	Y	N
Lens 2A	50	N	Y
Lens 2B	100	N	N
Lens 2C	10	N	N
Deflector 3X	25	Y	N
Deflector 3Y	25	Y	N
Inner Hemisphere	20	N	N
Hoop 1	20	N	N
Hoop 2	20	N	N
Hoop 3	10	N	N
Hoop 4	10	N	N
Outer Hemisphere	10	N	Y
Deflector 4X	25	Y	N
Deflector 4Y	25	Y	N
Lens 3B	100	N	N
Lens 3C	50	N	Y
Deflector 5X	25	Y	N
Deflector 5Y	25	Y	N
Lens 4B	200	N	N
Deflector 6X	25	Y	N
Deflector 6Y	25	Y	N

Each voltage supply included a voltmeter to monitor the potential on each lens/deflector, while several supplies (Anode, *L1C*, *L2A*, the outer hemisphere and *L3C*) also contained ammeters to monitor the electron beam current at various points throughout the monochromator. The readouts from all of the voltmeters and ammeters were displayed simultaneously at the PC (Figure 2.3.7).

The voltage supplies for the monochromator were soldered into an in-house made break-out box where they were cross-referenced (Figure 2.3.8). From the break-out box the floated supplies connected directly to the appropriate monochromator element using a multicore cable, soldered into a pair of 36-pin Amphenol vacuum feedthroughs on 2³/₄" flanges. Inside the collision chamber the feedthrough pins were finally connected to their corresponding monochromator elements using 20 AWG solid core, Teflon coated wire (Thermax) and gold plated wire connectors (Farnell 365-2002).

The picoammeters for the Faraday cups were also connected to the Amphenol feedthroughs with RG-58 coaxial cable (Belden). The voltage output of each picoammeter was connected to the PC using to a 12-bit, 8 input Analog-to-Digital converter (LabJack U12), interfaced via the USB port, to allow the PC to log the cup currents.

Protection from Electric and External Magnetic Fields

The inside of the collision chamber was lined with stress annealed Co-Netic shielding in order to prevent terrestrial magnetic fields from influencing the operation of the monochromator. When the chamber was closed this shield formed a ‘can’ which completely encompassed the collision chamber, except for some holes which were cut through the shield to act as gas and pumping ports. With the Co-Netic shield in place, the magnetic field, measured using a digital magnetometer (Schonstedt DM 2220) along all three orthogonal axes and at a number of different locations within the collision chamber, never exceeded 5 mG. Further, the field was less than 1 mG in the vicinity of the hemispheres, where the electrons have the least kinetic energy and are therefore most susceptible to

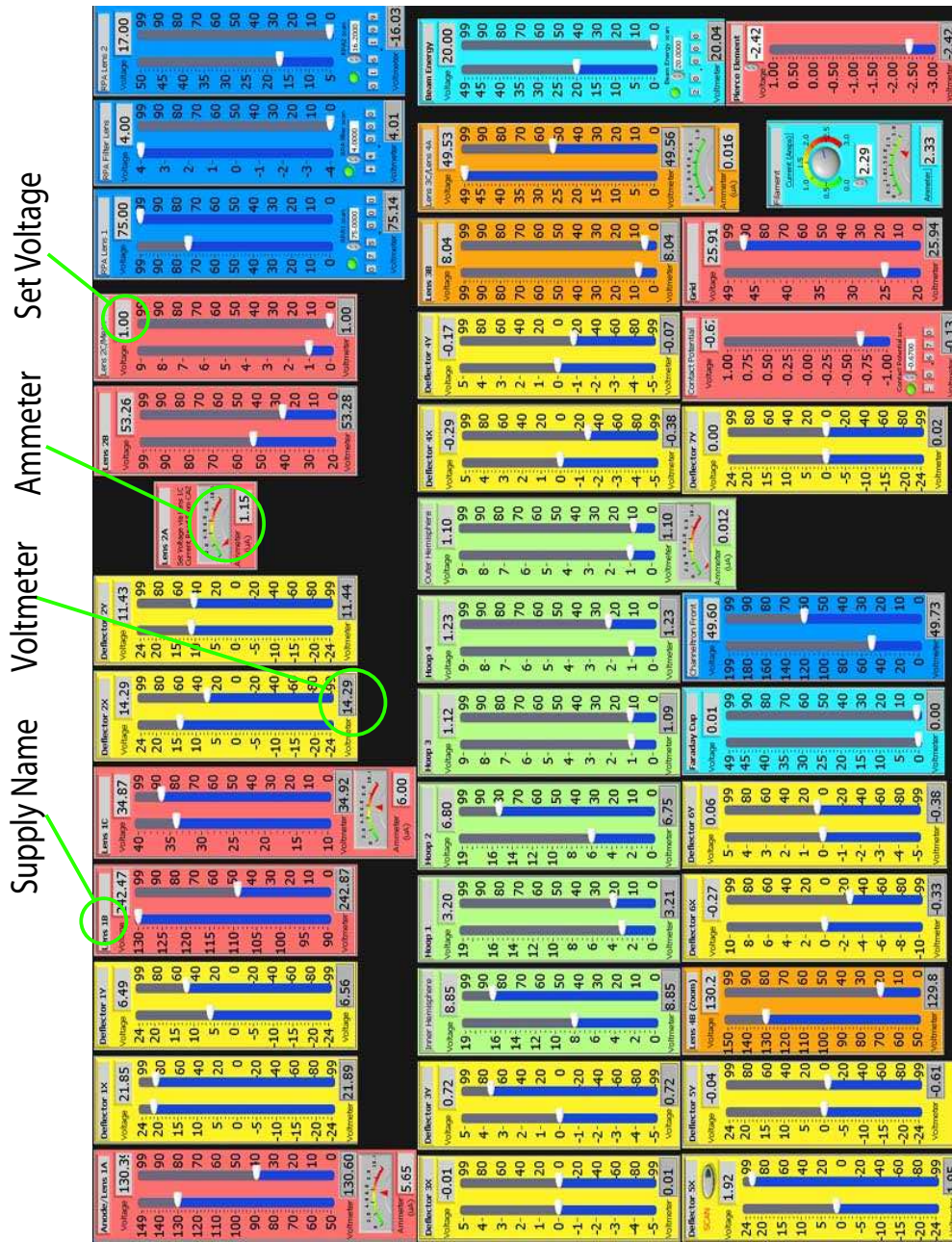


Figure 2.3.7: Screenshot of the monochromator-computer interface. The potentials supplied to all the monochromator elements can be seen to be simultaneously displayed. Similarly, the relevant ammeter readings can also be seen.

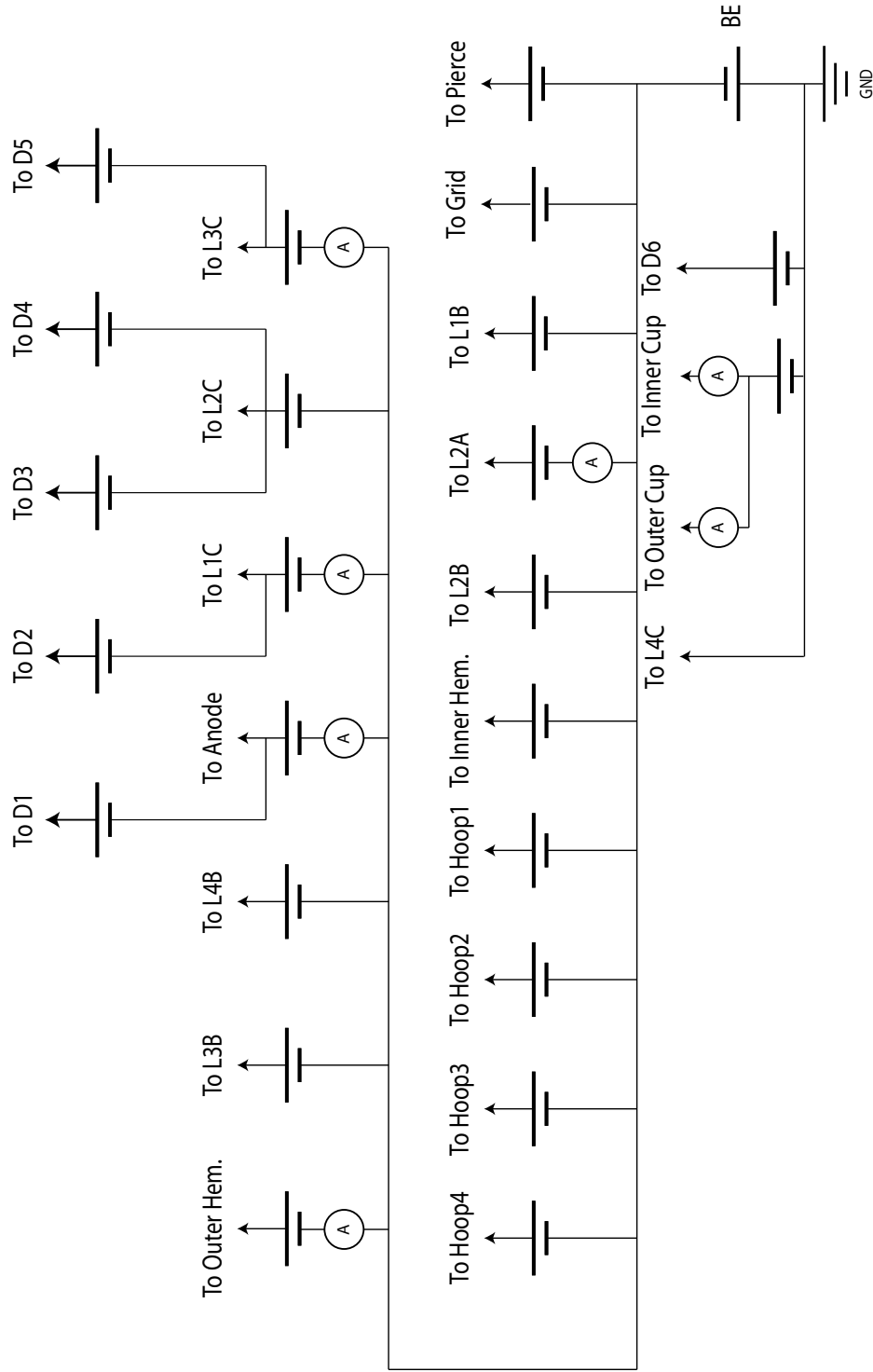


Figure 2.3.8: A schematic diagram showing how the monochromator's voltage supplies were floated at the breakout box. BE (beam energy) denotes the cathode potential. The arrows denote a direct connection to the relevant monochromator element.

deflection by stray magnetic fields.

Since the electron monochromator was completely contained within a differential pumping housing, with only the grounded final lens element protruding into the collision chamber, the interaction region was free from stray electric fields caused by the potentials placed on the electron optics of the monochromator. To prevent the potentials for the CEMs and RFAs from penetrating into the interaction region their connecting wires were surrounded by a stainless steel cover, which sat on the electron detection array. These wires were also covered in Al foil, between the vacuum feedthrough and the cover, to ensure that the potentials on them did not have line-of-sight to the interaction region at any point.

Monochromator Cleaning and Baking Procedures

The electron monochromator baseplate and hemispheres were baked by two separate thermocoax heaters. The first heater was mounted in a copper block fixed to the baseplate (Figure 2.3.9), while the second was seated in a groove cut around the equator of the outer hemisphere (Figure 2.3.4). These thermocoax heaters were each powered by a 30 V, 3 A, DC power supply (Topward Electric Instruments TPS-400). The temperature of the baseplate heater was monitored using K-type thermocouples. A temperature controller, manufactured in-house, was used to control the temperature of the baseplate. This was achieved in the following way: (1) The controller monitored the baseplate thermocouple readout and switched off the power supplies to both heaters when the baseplate temperature reached 105°C; (2) both heaters were then switched back on again when the baseplate temperature reduced back to 100°C. As such, a stable baseplate temperature, between 100°C and 105°C, was maintained over prolonged periods of baking. The monochromator was typically baked over 24 hours, after exposing the collision chamber to atmosphere.

In addition to the thermocoax heaters, both the cylindrical and aperture lenses were baked by a single EHJ-type halogen lamp (Figure 2.3.9). This lamp was powered by a 40 Volt, 12 Ampere, DC power supply (Rowan Electronic

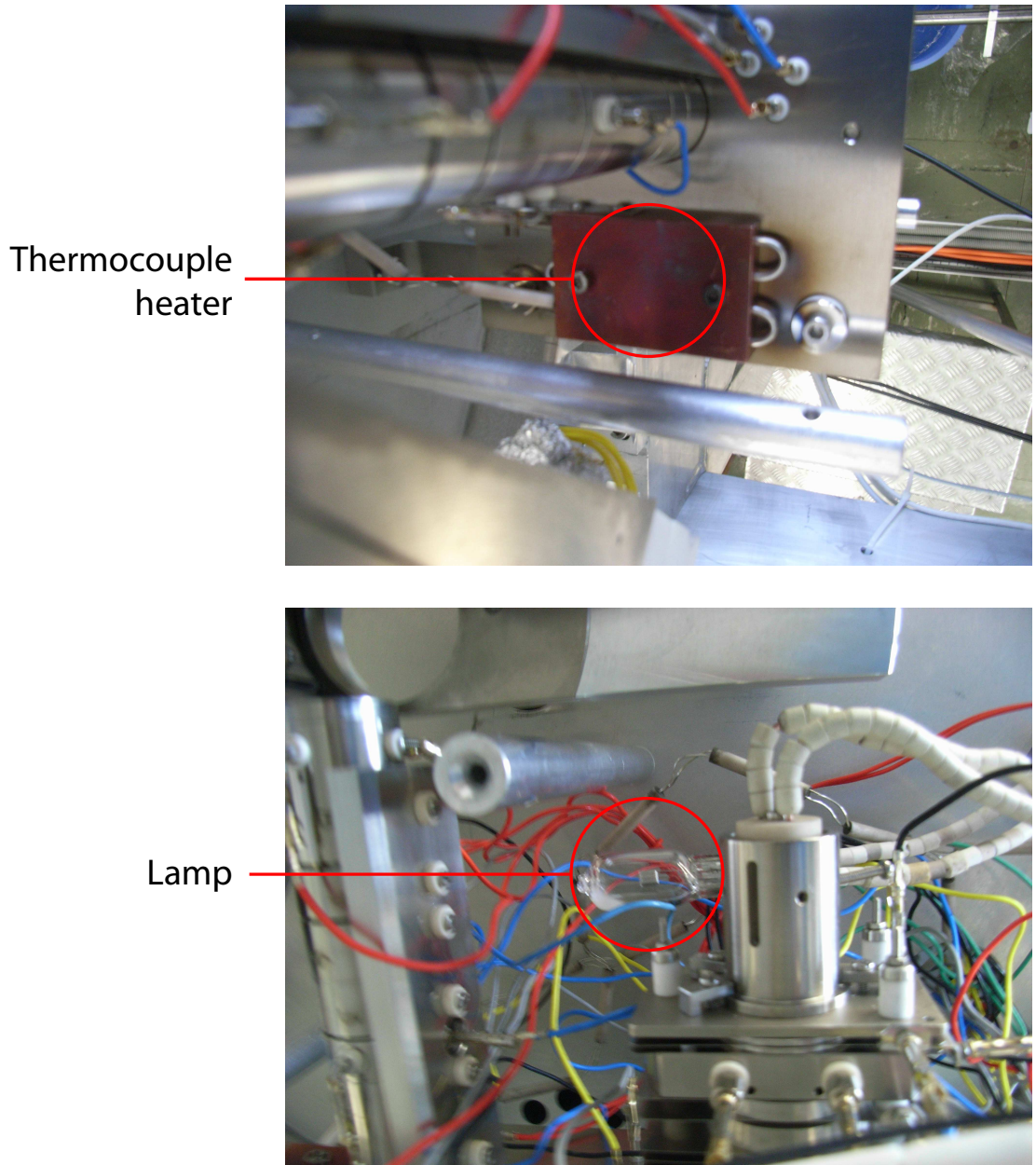


Figure 2.3.9: A photograph showing of the baseplate heater and the halogen lamp.

Measurements). The lamp, rated at 24 V and 240 W, was typically run at 10 V, 60 W in order to increase the lifetime of the filament and to preserve the Teflon coated monochromator wires, which were rated to 150°C. The temperature of *L4C* was recorded by a second K-type thermocouple to monitor the heating effect of the lamp, which typically ranged between 100-110°C with the lamp at 60 W.

In addition to baking, approximately once every year the monochromator was removed from the chamber in order to clean any surface contaminants from the lenses and apertures. The cleaning procedure consisted of removing the monochromator from the chamber and disassembling both lens stacks. The lenses and apertures were then polished with fibre optic paper, and then reassembled. The entire process, including dismounting and reinstalling the monochromator, was usually completed within one day.

Monochromator Operation

The electron beam energy was in principle determined by setting the cathode potential corresponding to the desired incident beam energy and having *L4C* earthed to the chamber. A 1 V contact potential supply was placed between the centre of the filament and the beam energy supply to accommodate for the difference in the work functions between the hot tungsten filament and the cooler titanium surfaces of the surrounding lenses and apertures. Table 2.2 summarises the theoretical operating potentials for the monochromator's lenses [46], fringe field correcting hoops [47] and hemispheres [48], with all of these supplies referenced to the cathode potential. In practice the theoretical settings, for both the aperture and cylindrical lenses, were used as a starting point from which to manually optimise the monochromator, rather than as the actual working settings. The potentials which actually optimised the monochromator's performance deviated significantly, in some case by as much as 100%, from the theoretical values. The reason for these discrepancies is that a real monochromator has some practical limitations, such as impurities on the lens surfaces and space charge broadening effects that are not considered by the

Table 2.2: Theoretical and typical operating potentials for the electron monochromator’s lenses, hoops and hemispheres, for an electron beam into the interaction region of 20 eV. All potentials are in Volts and given with respect to the cathode potential. Note that in reality the *L4C* potential corresponded to real earth. A, B and C denote each of the lens elements as the electrons move away from the filament.

	L1		L2		L3		L4	
	Theory	Actual	Theory	Actual	Theory	Actual	Theory	Actual
A	100	144	20	24	6	6	14	50
B	240	186	41	85	20	47	60	200
C	20	24	6	6	14	50	20	20
	Outer Hem.	Hoop1	Hoop2	Hoop3	Hoop4	Inner Hem.		
	10.00	7.69	6.84	5.24	4.56	3.60		

theory. Therefore, typical working values for the monochromator potentials are also given in Table 2.2. The potentials for the deflectors typically varied between -2–2 V, with respect to the potential on the relevant field-free region.

The pass energy for the monochromator was typically 6 eV, with the theoretical potentials for the Hoops [47] and Hemispheres [48] also being given in Table 2.2. The actual potentials applied to the hoops and hemispheres typically did not deviate from these theoretical values. At a pass energy of 6 eV the theoretical energy resolution of the present monochromator is ~ 70 meV [49]. Realistically this value is a lower bound to the practical energy resolution, as the theory gives no consideration to effects such as space charge broadening in the hemispheres, or linear magnification effects from *L2*. Both of these latter effects will degrade the achievable resolution of the monochromator.

The monochromator’s output current was optimised by monitoring the inner and outer cup currents and aiming to simultaneously maximise:

$$I_{tot} = I_{inner} + I_{outer} \quad (2.3.1)$$

$$\%_{focus} = \frac{I_{inner}}{I_{tot}} \times 100. \quad (2.3.2)$$

The Faraday cups were also used to monitor any variations in the monochromator's output current or focus during an experimental run. In practice, the $\%_{focus}$ typically ranged between 50% and 90% depending on the incident energy of the electron beam, with the focus improving as the incident electron energy was raised. Total beam currents were typically between 1 - 5 nA at 6 eV pass energy, but could be increased to as high as 20 nA by increasing the pass energy to 10 eV. As with the beam focus, the current at the Faraday cup increased as the incident electron energy was increased.

A small positive potential, typically 10 V with respect to ground, was occasionally applied to the Faraday cups to help tune the monochromator. This typically occurred if the output current was small or the electron beam was poorly focussed. During an experimental run however, the Faraday cups were always kept at ground potential.

At incident energies below ~ 15 eV, the electron beam current measured at the Faraday cups reduced to zero, regardless of what potentials were applied to any lens/deflector elements of the monochromator and even when a positive potential applied to the Faraday cups. Extensive efforts (see earlier) were made to try and optimise the monochromator's output at the lower energies, however, the performance did not improve. Experiments at incident energies below 15 eV were therefore not performed using this apparatus. However, above this incident energy the monochromator's performance was more than adequate for the scattering experiments to be conducted, with data acquisition typically taking < 4 hours.

Finally, one of the novel instrumental developments of this project is highlighted. The monochromator control software featured an autotuning facility, so that the optimal potentials for the lenses and deflectors were determined by the computer. This facility, discussed in detail in Appendix B, was much faster at finding optimal potential settings than manual tuning, and significantly improved the output current and stability of the monochromator, at incident energies above 15 eV.

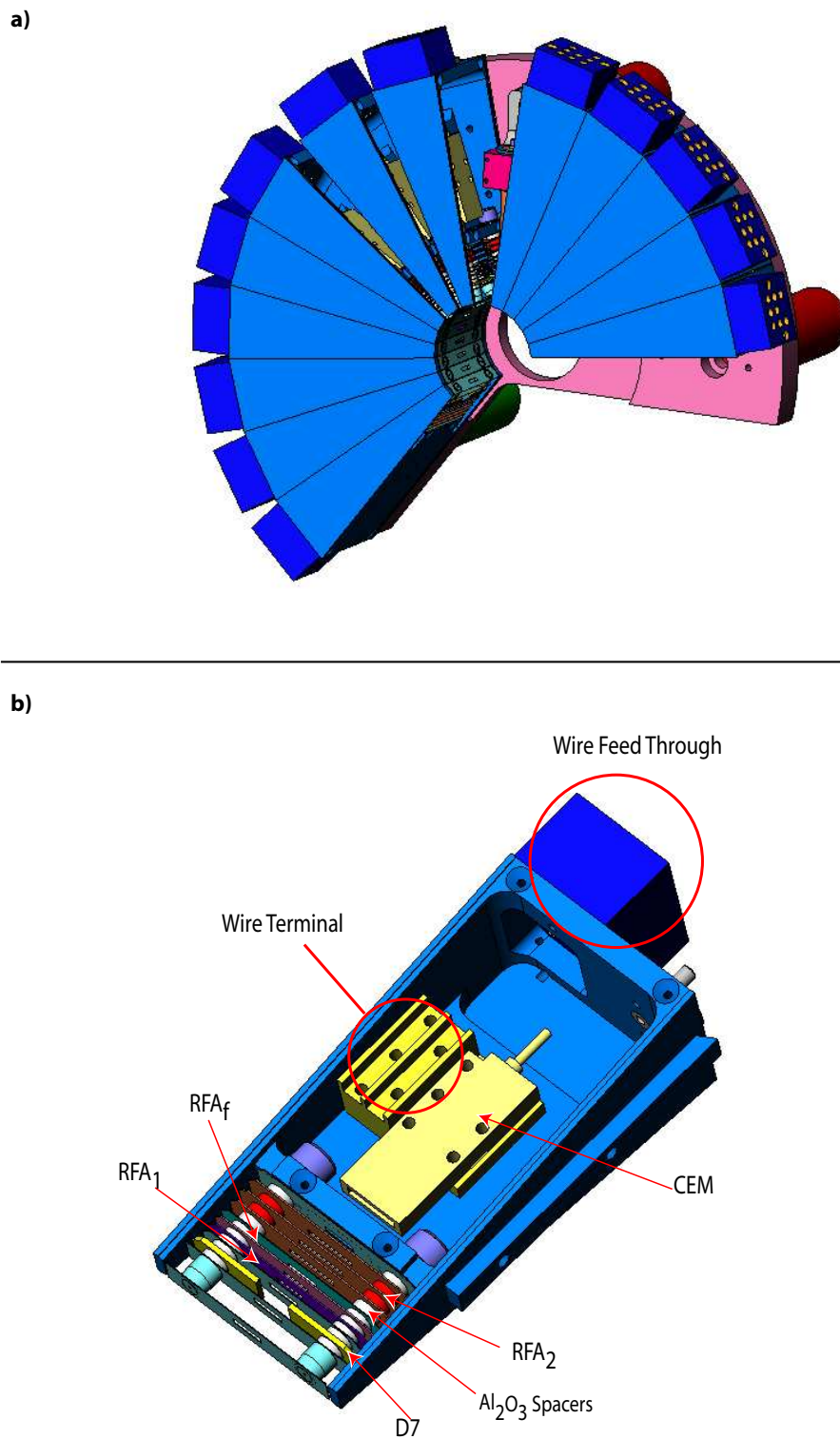


Figure 2.3.10: Pictorial representation of a) the multi-detector electron analyser array and b) one of the analyser wedges.

2.3.2 Electron Detectors

Elastically scattered electrons were detected by an array of thirteen individual detection units, each containing a SJUTS KBL210 channel electron multiplier (CEM) and a retarding field analyser (RFA) (Figure 2.3.10). This configuration was chosen to allow entire angular distributions of scattered electrons, at a given energy, to be collected simultaneously. This enabled a significant saving in data acquisition time versus systems that employ a single detector rotating around the interaction region.

Each RFA and CEM was mounted within an individual wedge shaped housings. Thirteen of these wedges being were directly to a baseplate, that was in turn bolted to the chamber wall. The baseplate was insulated from the chamber by PTFE spacers to allow it to be floated at a potential other than ground, if required. During the current work, however, the baseplate was always grounded. The analyser wedges covered an angular range of -75° to 135° . Each analyser had an angular field of view of $\approx 5^\circ$ and was located 20 mm away from the centre of the interaction region.

Retarding Field Analysers

The RFAs had aperture parallel-plate-type geometries (Figures 2.3.10 and 2.3.11), and their original design was modelled using Simion 6.0 at the ANU. Scattered electrons entering an analyser were steered onto the entrance plane of the CEM by a single deflector set ($D7$). These electrons were then focused onto the CEM entrance by a two element, aperture-type lens (lens elements RFA_1 and RFA_F). Finally, the electrons were energy analysed with the third of the RFA lenses (RFA_2), before impacting onto the CEM.

The analyser lenses were made from 0.15 mm thick titanium sheets and contained slits that were 1.4 mm in width and of varying length (detailed in Figure 2.3.11), to allow passage of the electrons. Successive lenses were separated by hollow Al_2O_3 spacers (Small Parts). The RFAs were held together by two grounded

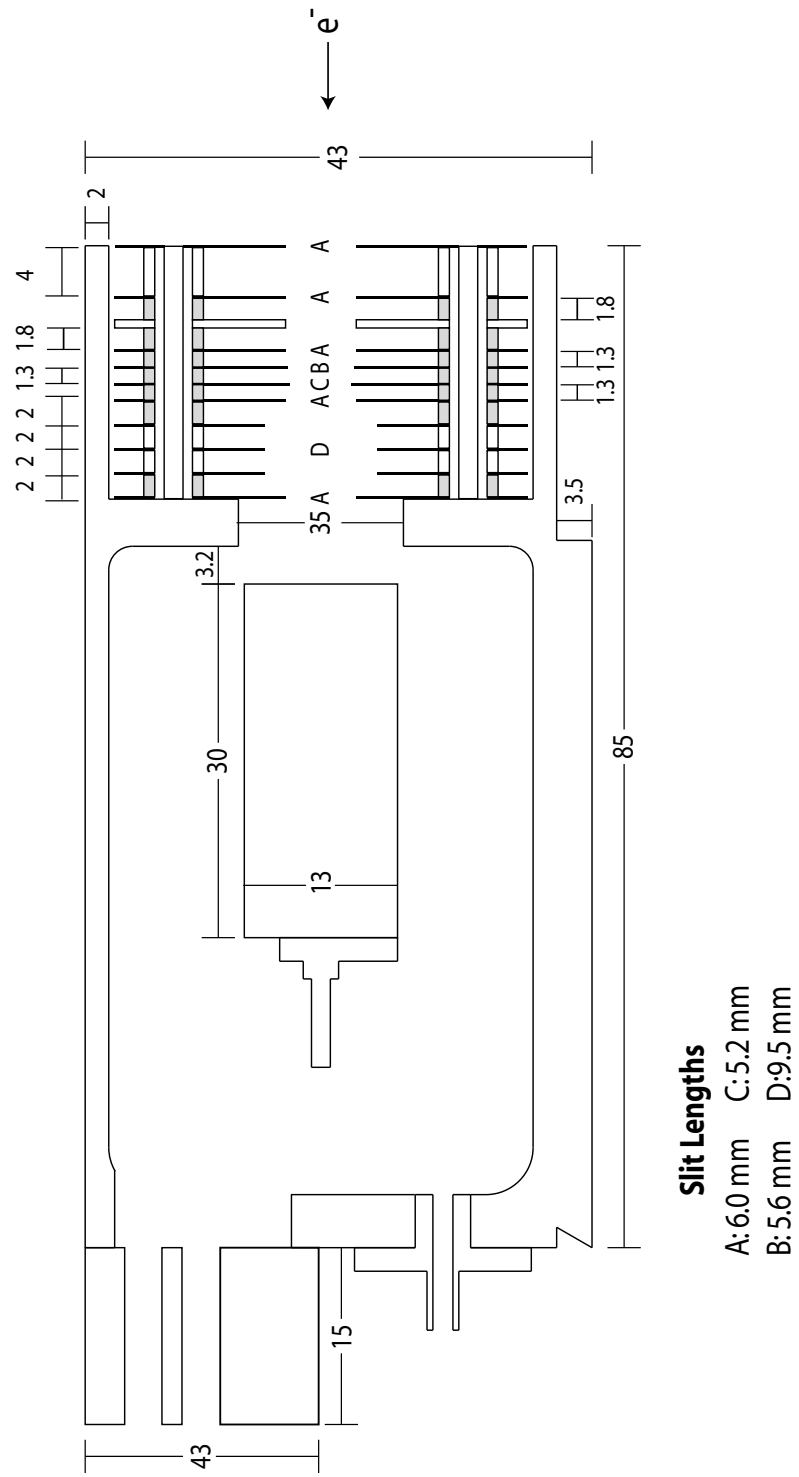


Figure 2.3.11: A schematic diagram of one of the analyser wedges. The dimensions are all in mm.

stainless steel posts with the first grounded lens welded to the end of the posts, and the posts themselves running inside the Al_2O_3 spacers.

Detector Electronics

The potentials to the RFAs, *D7* and the CEM-front were generated by custom made, computer interfaced voltage supplies similar to the electron monochromator supplies. Note that these supplies were wired to their respective lenses via a 20 pin Amphenol vacuum feedthrough. The high voltage (HV) applied to back of each CEM was generated by a stand alone high voltage power supply (Danfysik N 1150). An electrical schematic of the present arrangement is given in Figure 2.3.12.

The front face of the CEM typically operated at a potential in the range of 50–100 V, again with respect to ground, with this small positive potential at the entrance plane of the CEM preventing detection of any positive ions and optimising the detection efficiency of the CEM. The rear of the CEM typically operated at 2.5 kV with respect to ground, creating a positive bias for electrons cascading through the CEM. At a bias of 2.5 kV, the CEMs typically output a 20 mV pulse of approximately 8 ns in duration, when impacted on by an electron.

Within the collision chamber the output pulses were connected to a series of 3 pin, MDC high voltage feedthroughs using coaxial cable. Outside the vacuum chamber the output of each CEM was decoupled from the high voltage using 150 pF capacitors. The decoupled output pulses were then preamplified, amplified and converted to +5 V TTL pulses using a set of in-house constructed preamplifiers and comparators (Flinders University, School of Chemistry, Physics and Earth Sciences Electronics Workshop). These TTL pulses were passed to a commercially purchased break-out box (NI-BNC 2121) via $50\ \Omega$ through-terminators and coaxial cable. From the breakout box the TTL pulses were registered by one of four PCI counter/timer cards (NI-PCI 6602) housed in the data acquisition PC. Each 6602 card contained eight counter/timers, for a total of 32 counters.

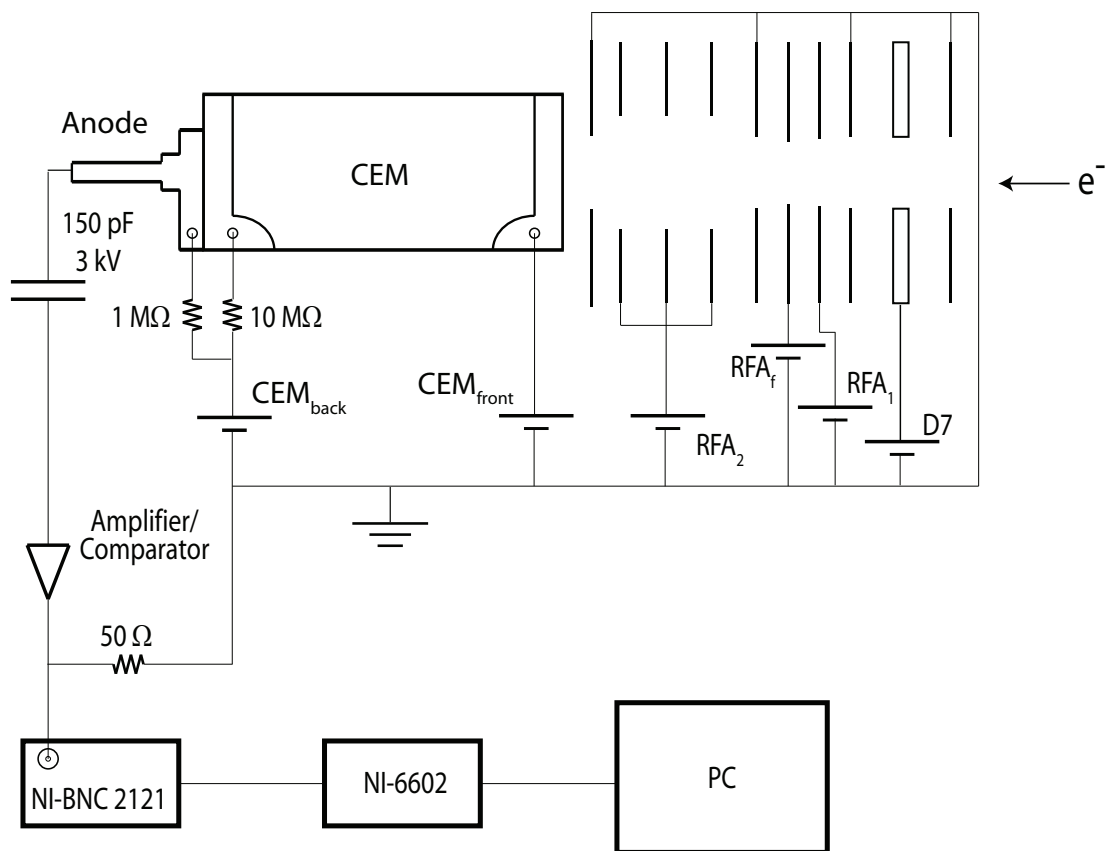


Figure 2.3.12: A schematic diagram of the electronics used for the electron detectors and analysers.

RFA Operation

The RFAs filtered the electrons based on their kinetic energy in the axial direction of the analyser, by retarding the elastically scattered electrons with an axially directed electric field. An electron of energy $E_e = qV_e$ (where q is the electron's charge and V_e is the electric potential) passed through RFA_2 providing that $V_e > V_A$, where V_A is the potential on RFA_2 , with respect to ground. Otherwise, the electron was repelled away from the CEM and not detected.

The energy resolution of the RFAs was minimised by ensuring the electrons were well collimated in the axial direction of the analyser. Thus, the potentials on RFA_1 and RFA_f , which formed a two element lens, were important for optimising the energy resolution of the analyser. RFA_1 and RFA_f typically operated at potentials of 94 V and 3 V respectively, relative to ground, which optimised the electron count rate across the thirteen analysers over a range of electron beam energies.

The energy resolution of RFA_2 also depended on the aperture size. The minimum energy resolution (ΔE_A) of an aperture-type RFA, assuming that the electron's velocity has no component in the transverse direction of the analyser, is given as:

$$\frac{\Delta E_A}{E_A} = \sin^2 \left(\frac{r_0}{4d} \right), \quad (2.3.3)$$

where E_A is the analyser pass energy, r_0 is the radius of the RFA aperture and d is the distance over which the electrons are retarded [50].

Since the present configuration used rectangular slits rather than circular apertures, the longest side of the slit was taken as the effective radius in order to calculate the limiting energy resolution. The length of the slit in RFA_2 is 9.5 mm (an effective r_0 of 4.75 mm), and the distance between the final grounded lens and the centre of lens RFA_2 was 4.12 mm. Using the above definition, the minimum energy resolution of the RFAs was $\Delta E/E=0.061$, or 1.2 eV at an analyser pass energy of 20 eV. In practice, the RFAs achieved an only slightly lower energy resolution of $\Delta E_A/E_A=0.065$, indicating the scattered electrons were indeed

well collimated by RFA_1 and RFA_f before entering RFA_2 . Typically therefore, RFA_2 was set 4 V positive with respect to incident beam potential, to ensure all elastically scattering electrons were transmitted to the CEM. Details of the experiments to measure the energy resolution of the analysers are described in Appendix C.2.

The energy level of the first vibrationally excited state in polyatomic molecules may be as low 25 meV [15], and is still around 200 meV for even simple diatomic molecules such as nitrogen. Thus, the present RFAs were unable to resolve vibrationally inelastic electrons from those which were due to vibrationally elastic scattering. However, with the exception of energy regions where resonances are significant in the scattering process, the contribution to the elastic signal from vibrationally inelastic electrons will be small, typically less than 1% [7]. The RFAs present energy resolution is, however, generally sufficient to discriminate against electronic excitations, which are typically of the order of several electron-volts or more in magnitude.

2.3.3 Data Acquisition and Analysis Protocols

Data acquisition was performed under computer control, using the PC (2 GHz, Pentium 4, Windows XP) housing the four 6602 counter/timer cards (Section 2.3.2). Each of these cards contained 8 counter/timers, which were used to simultaneously register the amplified output pulses from the 13 CEMs. The output from each of the individual CEMS was registered by two counters on one of the PCI-6602 cards. Using a 12-bit, 8 input analog-to-digital converter (NI 6608) the data acquisition PC also recorded the Faraday cup currents, the stagnation pressure behind the nozzle and the collision chamber pressure during an experimental run. All of the data acquisition software was written using a LabView 8.0 platform.

The timing protocol for the experiment was dually controlled by a timing controller, which was manufactured in-house (Flinders University, School of

Chemistry, Physics and Earth Science Electronics Workshop), and the PCI-6602 counter/timers. The timing controller had six available outputs, each of which output 5 V TTL pulses at a programmable time delay from an internal timing pulse. The timing controller was capable of a timing resolution of ≈ 750 ps.

Time control of the DCS scattering measurements was as follows; One channel of the timing controller was designated as the master time pulse (MTP) and was used to trigger the pulsed nozzle driver. The MTP was also registered by the PCI-6602 counter/timers, and counting of output pulses from the CEMs was gated according to the MTP. Following detection of the MTP, electron counts were accumulated in a 5 ms window, corresponding to the time when the gas pulse passed through the electron beam. A small delay ($400\mu\text{s}$) was typically used between detection of the MTP and the opening of the counter gates, to allow for the response time of the pulsed nozzle driver and the transit time of the gas pulse to the interaction region. After a further 55 ms delay, to wait for the gas pulse to pass through the interaction region, the counter gates were then reopened for 5 ms to accumulate background counts. Thus, both signal counts (electrons elastically scattered by the molecular beam) and background counts (electrons elastically scattered by background gases) were collected during one experimental run. The pulsed nozzle driver and counters were triggered at a frequency of 10 Hz by the timing controller.

Signal and background counts were accumulated over several minutes before they were binned by the computer, whereupon a new bin was started. At the start of any time bin, the Faraday cup current, stagnation pressure and collision chamber pressure were all recorded. Each of these values was subsequently rerecorded at the end of each time bin, to check for any variation. All these data were stored together with each bin so that, if any of the experimental conditions varied significantly during a run, each bin could be normalised by the appropriate value. In practice however, the system was generally sufficiently stable that independent bin-by-bin normalisations were not required to any significant degree. The time bins were typically between 5–10 minutes in duration, while the total

accumulation time typically ranged from 1–4 hours depending on signal levels.

Error Analysis

The final value of the elastically scattered electron count rate (\dot{N}^e), for both the signal and background, was evaluated by taking a mean of the scattered electron count rates across all of the time bins and for each discrete scattering angle. The uncertainty in both of these scattered count rates ($\delta\dot{N}^e$) was then determined as the standard error in this mean:

$$\delta\dot{N}^e = \frac{\sigma}{t\sqrt{N}} \quad (2.3.4)$$

where σ is the standard deviation between the bins, t is the total accumulation time and N is the total number of bins. The true signal count rate at each scattering angle was then evaluated as the difference between the signal and background count rates, and the total uncertainty calculated as the quadrature sum of the individual uncertainties in the signal and background count rate.

This approach was adopted so that the count rate uncertainty included the variation in the scattered electron counts due to (i) pulse-by-pulse variations the gas pulse density and (ii) the statistical variation (evaluated as the square root of the counts). The pulse-by-pulse beam density variation is inherent to the use of pulsed gas sources, and in the present apparatus was estimated as 200% of the mean gas density. Data acquisition usually continued until the uncertainty in the counts, across all of the detectors, had reduced to less than 5%.

2.4 Time-of-Flight Mass Spectrometer

The time-of-flight mass spectrometer (TOFMS), was a Wiley-McLaren [51] orthogonal-acceleration type TOFMS (Figure 2.4.1). Molecules entering the TOFMS were single-photon ionised by 118 nm radiation from a twice frequency tripled Nd:YAG laser. Ions were accelerated orthogonally out of the beam by an electric field, and then entered an electric field-free flight region. Lighter ions entered the field free region with a higher velocity than heavier ones, and hence

they spatially separate according to mass as they traversed the flight region. Once through the flight region, the ions impacted onto a detector and their mass was determined according to the time of flight.

2.4.1 Ion Extractors

Experimental Configuration

Ions in the TOFMS were accelerated orthogonally to the direction of the target beam by an electric field. The electric field was formed by potentials placed on two 0.5 mm plates, denoted as the extractor and repellor. The field uniformity between the extractor and repellor plates was maintained by nine additional 0.5 mm plates. The extractor and repellor rings were separated by 55.8 mm, and the plates were held together by eight grounded aluminium rods. Successive plates were separated by 5.08 mm Al_2O_3 spacers (Small Parts). The plates were connected to one another by a chain of $1\text{ M}\Omega$ glass-coated resistors (Ohmite, RX-1M Hi-Meg), to form an approximately uniform electric field between the repellor and the extractor. To further improve field uniformity, high transmission molybdenum mesh was spot welded over the extractor.

Once the ions were past the extractor they were accelerated up to the final grounded plate. This grounded plate also had a molybdenum mesh spot welded over it in order to optimise field uniformity and was located 55.8 mm from the extractor. Nine successive rings up to the ground ring, separated by Al_2O_3 spacers, were connected by $1\text{ M}\Omega$ resistors to maintain the uniformity of the electric field. Once the ions had passed the grounded ring they entered the region of field free flight where they continued to separate by mass.

The potentials applied to the extractor and repellor were supplied by two HV power supplies (Fluke 415B), connected to a 4 pin SHV vacuum feedthrough by RG-58, C\U type coaxial cable (Belden). Within the TOF chamber the field rings were wired with 20 AWG, Ag Teflon coated wire (Thermax). Since the ions

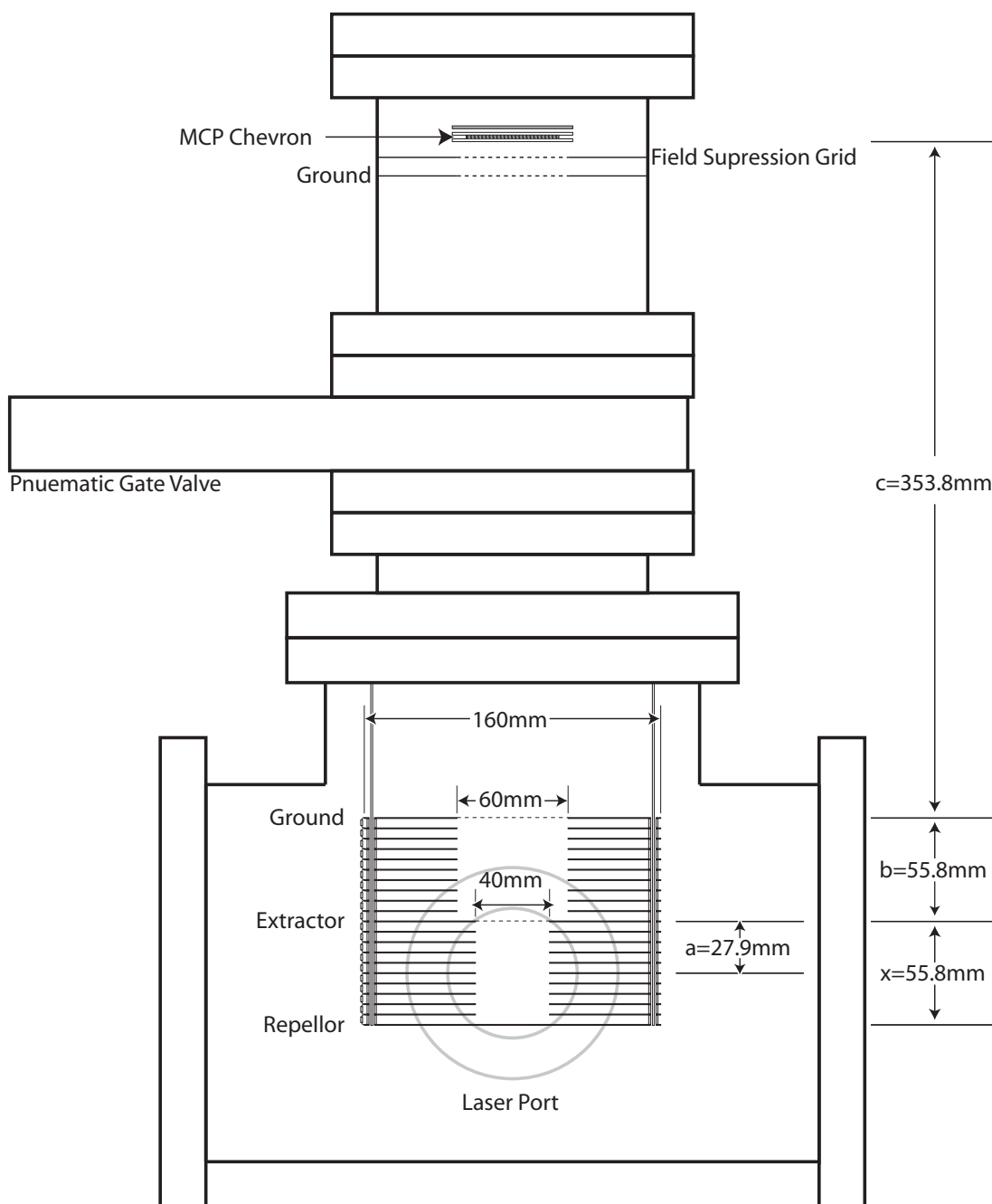


Figure 2.4.1: A schematic diagram of the present TOFMS.

were formed in the centre of the field rings by the laser, the HV to the extractor, repeller and MCP detectors was continuously applied.

Space Focussing

To optimise the mass resolution of the TOFMS, the geometry of the TOFMS was designed for a second-order space focus. Space focusing means that an ion's time of flight is, to a second-order approximation, independent of that ion's initial position within the TOFMS. Space focusing exploits the fact that ions formed closer to the repeller enter the field free region with a higher velocity than those that originate further away, since they spend a longer time in the extraction region. If the geometry and potentials on the extractor and repeller are set appropriately there is a unique point in the flight tube, referred to as the 'space focus', which all ions of equal mass reach at the same time. By locating the ion detector at the space focus, the TOFMS mass resolution was optimised by removing the time spread of ions arriving at the detector due to the width of the gas beam and ionising laser. The potentials and field ring geometry required for a space focus are given in the following two equations [52]:

$$a = \frac{c - 2b}{2(c + b)} \left[c \left(\frac{c - 2b}{3c} \right)^{\frac{3}{2}} + b \right], \quad (2.4.1)$$

$$V_{Ex} = 2V \left(\frac{c + b}{3c} \right). \quad (2.4.2)$$

In equation (2.4.2) V and a are the potential and distance to the extractor, respectively, from the point where the ions nominally originate and V_{Ex} is the extractor potential. Note that all the other variables in equations (2.4.1) and (2.4.2) are defined in Figure 2.4.1. The repeller potential, V_{Rp} , is related to V and V_{Ex} by:

$$V = V_{Ex} + \frac{a(V_{Rp} - V_{Ex})}{x}, \quad (2.4.3)$$

with x the distance between the extractor and repeller. In the current work, the space focus was located a distance of 356 mm from the field rings, with typical potentials $V_{Rp}=2500$ V and $V_{Ex}=1576$ V applied to the field rings.

2.4.2 Photoionisation Source

Ions were created in the TOFMS through photoionisation of the molecular beam. The photon source was a 2 W, Q-Switched Nd:YAG laser (Quantel BrilliantB), which produced output pulses 5 ns in duration. The fundamental YAG output (1064 nm) was frequency tripled to produce 355 nm output light using non-linear optics, sourced from a commercially purchased third harmonic generation unit (Quantel) mounted to the front of the YAG. The output from the first tripling stage of the YAG was passed through a frequency tripling cell that contained a phased matched mixture of Xe and Ar, to produce photons of wavelength 118 nm. Generation of 118 nm photons in phased matched mixtures of inert gases has been previously discussed by several authors [53, 54]. The 118 nm radiation was then focused onto the target beam and the required ions were produced by single photon ionisation (SPI).

SPI occurs when the energy of an incident photon is in excess of the first ionisation threshold of the target. A single 118 nm photon (10.48 eV) can ionise a variety of targets, however, it is typically not sufficiently energetic to cause the resulting cation to fragment. The efficiency of conversion of 355 nm UV to 118 nm VUV in the frequency tripling cell was estimated to be about 1% and thus two photon events, which may also lead to fragmentation, are unlikely due to the low 118 nm photon flux. The limitation of SPI, however, is that only species with a first ionisation threshold less than 10.48 eV were directly detectable in the TOFMS.

Experimental Configuration

The frequency tripling cell (Figure 2.4.2), was a stainless steel tube of 400 mm length and 25 mm inner diameter. The 355 nm radiation from the YAG was focused into the centre of the cell by a 200 mm focal length fused silica lens (CVI Laser PLCX-25.4-103.0-UV), which also sealed one end of the tripling cell. The 118 nm radiation was then focused into the centre of the field rings by a MgF₂ lens (CVI Laser BICX-25.4-102.4-MF) of 125 mm nominal focal length.

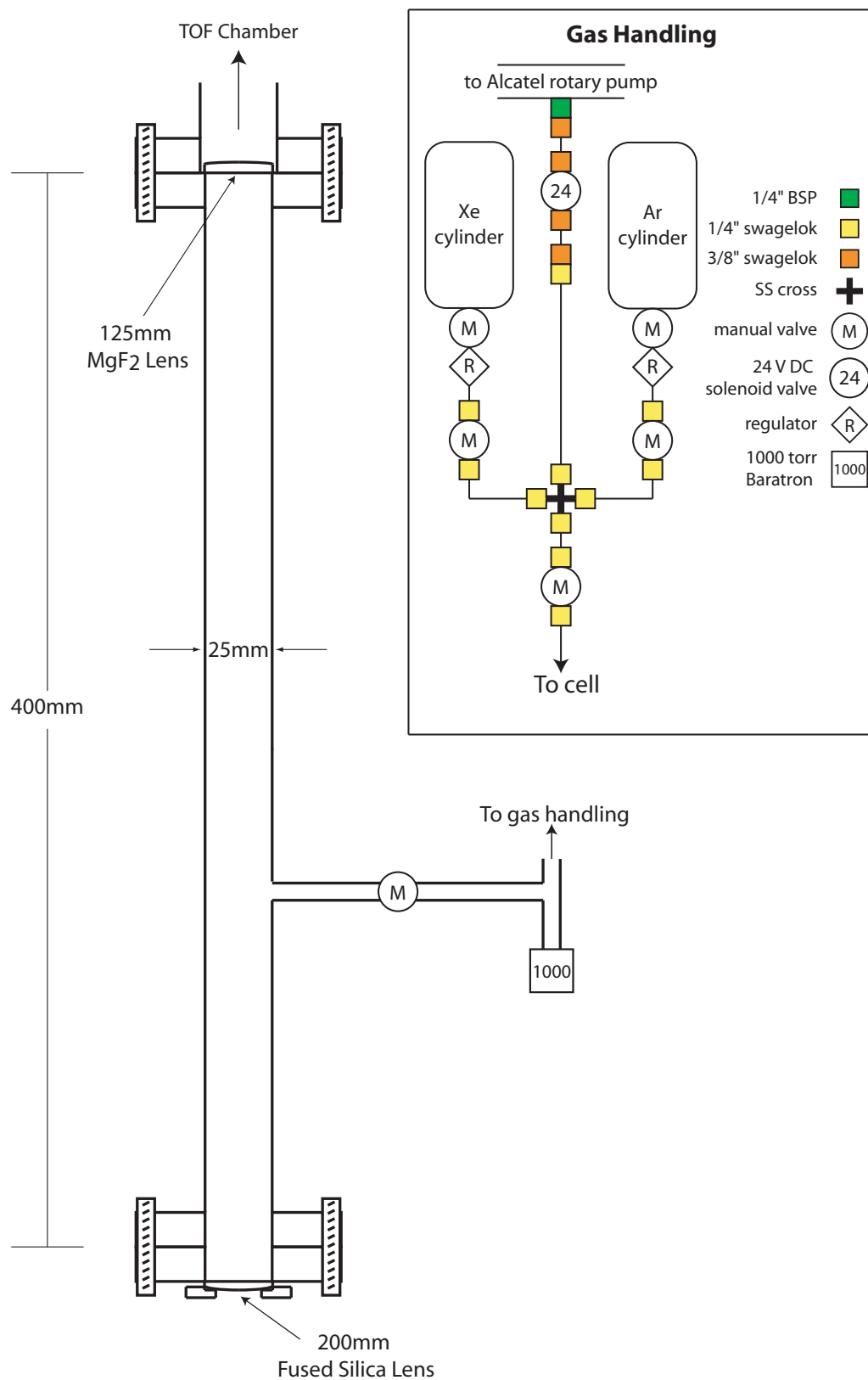


Figure 2.4.2: A schematic diagram of the frequency tripling cell, including the gas handling system.

The frequency tripling cell was evacuated by using the Alcatel rotary pump, while the pressure in the cell was monitored by a 1000 Torr Baratron (MKS 127A). The cell was evacuated and filled through a small gas handling system (Figure 2.4.2). The partial pressures in the frequency tripling cell were typically 5 Torr of Xe and 55 Torr of Ar. The experiments which were conducted to optimise these pressures are described in Appendix C.3.

2.4.3 Ion Detectors

Ions produced in the TOFMS were detected at the end of the flight tube by two microchannel plate (MCP) detectors (Roentdek DET40) of 47 mm active area and arranged in a chevron configuration, with a timing anode. The front face of the MCP chevron was biased at -2800V, with respect to ground, using a high voltage supply (Danfysik N1130). A grounded electrode with a molybdenum mesh was placed 10 mm in front of the MCP chevron, to prevent the negative bias on the MCP front face perturbing the field free flight region. A second grid biased at -50 V with respect to the MCP front face was placed in between the MCPs and the end of the flight tube, 5 mm from the MCP front face. This secondary field suppression grid prevented the electrons which were formed at the entrance plane of the MCP chevron from accelerating toward the ground grid. The suppression grid was biased using the Danfysik N1130 HV supply. Both the MCP front face and suppression grid were wired to a HV vacuum feedthrough with teflon coated wire (Thermax), which was in turn connected to the voltage supplies by RG-58 coaxial cable.

With a bias of -2800 V, the MCPs output a -7 mV spike of 8 ns duration, when impacted by a single ion. This output was carried on 20 AWG Teflon coated Ag wire (Thermax) and terminated into $50\ \Omega$ at the vacuum feedthrough. The MCP signal then passed through the vacuum feedthrough and was connected by coaxial cable directly to a 4 channel digital storage oscilloscope (LeCroy Waverunner 6050), also terminated into $50\ \Omega$. The oscilloscope (DSO) typically acquired at 2 gigasamples per second. The DSO was controlled remotely by the

Pentium 4 PC, using LabView 8.0 software developed in-house. An electrical schematic of the present ion detectors is given in Figure 2.4.3.

2.4.4 Data Acquisition and Analysis

The present TOFMS was run by the timing controller described previously in Section 2.3.3. The YAG was triggered at a frequency of 10 Hz by this timing controller with the trigger pulses delayed 2 ms after the pulser trigger, so that the laser pulse intercepted the gas pulse in the TOFMS. The YAG trigger provided by the timing controller was also used to trigger the DSO sweeps.

The DSO traces were downloaded to the PC for analysis, with the DSO and PC connected through a 100 Mbps ethernet switch (NetGear FS108). Initially, an attempt was made to capture and download traces from the DSO to the PC on a shot-by-shot basis. However, as the DSO could not be used for data acquisition when transferring data to the PC, the maximum possible capture/download rate in those experiments was only 4 Hz. In order to increase this data acquisition rate, the DSO was typically used in sequence mode, in which the DSO was triggered at a rate of 10 Hz and traces were stored in the onboard memory of the DSO. Traces were subsequently downloaded to the PC fifty at a time. By operating in sequence mode, the overall acquisition rate was increased to 8 Hz, including dead time for data transfer. The individual waveforms stored on the PC were then averaged to form the final mass spectrum.

Individual traces from the DSO contained up to 100,000 data points, each point represented by 1 byte. Since the experiments typically contained up to 40,000 traces, the resulting data file could reach 4 Gb in size. To reduce the data storage space, traces were compressed using a run-length encoder (RLE) before being stored on the PC. The RLE averaged all points in each trace which were in excess of some threshold value (usually -2 mV) and stored these as a single value for the baseline. When an ion spike signal dropped below the threshold value, all

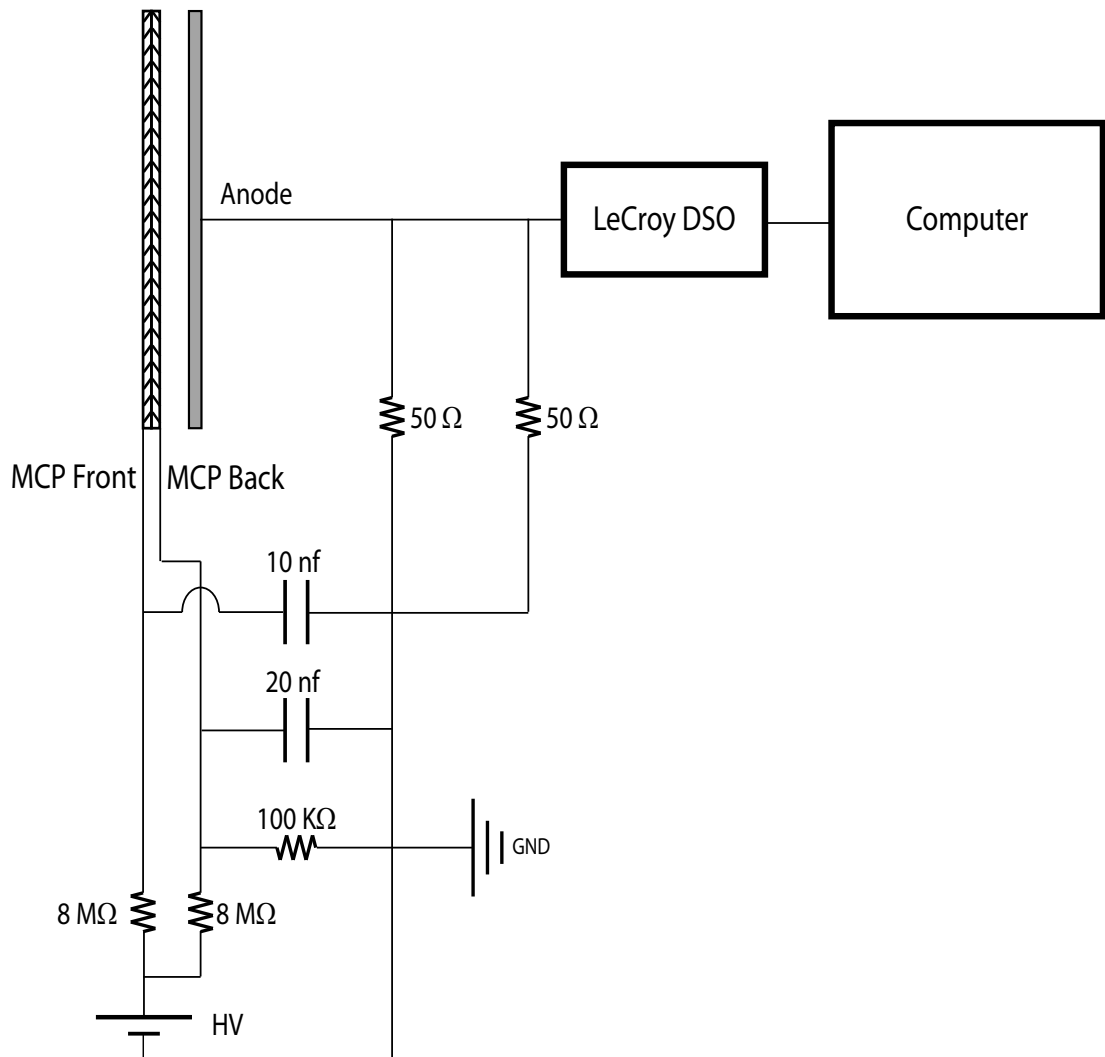


Figure 2.4.3: A schematic diagram of the electronics used for the TOFMS.

points in the spike were retained until the signal again exceeded the threshold. The points comprising the ion spike, plus the time location of the spike, were then stored on the PC. This compression process reduced the size of each trace from 100 Kb to as little as 100 bytes. As well as reducing data storage space, the RLE allowed ringing and other low lying electrical noise to be removed from the mass spectra, by setting the RLE's threshold below the amplitude of the noise.

Experiments to optimise and characterise the TOFMS are discussed in detail in Appendix C.3. At this point though, the mass resolution achieved by the TOFMS is highlighted, with the present configuration capable of resolving mass differences of one proton, over a range of molecular masses (up to 114 amu).